

1 **Variations in subsidence patterns in the Gulf of Mexico passive margin from**
2 **Airborne-LiDAR data and Time Series InSAR: Baton Rouge Case Study.**

3

4 **Carolina Hurtado-Pulido¹, Reda Amer², Cynthia Ebinger¹, Hayden Holcomb¹**

5 ¹Department of Earth and Environmental Sciences, Tulane University.

6 ²University of Missouri-St Louis, St Louis, Missouri

7 Corresponding author: Carolina Hurtado-Pulido (dhurtadopulido@tulane.edu)

8 **Key Points:**

- 9 • LiDAR differencing (1999-2018) and SAR time series (2004-2020) show similar spatial
10 variations. LiDAR documents horizontal changes.
- 11 • Subsidence varies between zones separated by growth faults and correlates with
12 groundwater level changes and fluid injection.
- 13 • Creep along the Baton Rouge growth fault likely accommodates spatial variations in
14 subsurface fluid levels.

15

16 **Abstract**

17 The Coast of Louisiana is affected by accelerating sea level rise compounded by land
18 subsidence, leading to land loss. Vertical crustal motions in the region are caused by natural and
19 anthropogenic processes that vary temporally and spatially across the Gulf of Mexico. We
20 investigate the role of growth faulting contributions to subsidence in a case study of Baton
21 Rouge, where two E-W striking, down-to-the-south normal faults, the Denham Springs and
22 Baton Rouge faults, cut compacted Pleistocene strata, and where sediment compaction should be
23 minimal. We used InSAR time series and LiDAR differencing data spanning 1999-2020 to
24 quantify modern vertical and horizontal displacements. After calibration with GNSS data, both
25 methods reveal similar spatial patterns in ground motion, with the faults delimiting areas with
26 different absolute rates. On average the area north of the Baton Rouge fault is subsiding faster
27 than the south, opposite to the long-term sense of fault slip. LiDAR mean vertical rates range
28 between -5 to -11 mm/y and -2.4 to -7 mm/y. InSAR time-series mean rates in the LOS direction
29 range between -10.9 to -13.6 mm/y and -8 to -10.6 mm/y, respectively, for the north and south
30 areas. Subsidence in the northern area likely is controlled by groundwater level changes caused
31 by pumping as indicated by groundwater extraction models. The southern area average is likely
32 influenced by the injection of fluids. Our results suggest volumetric changes caused by fluid
33 extraction and injection in regions separated by growth faults that are creeping to accommodate
34 the spatial variations in subsidence.

35 **Plain Language Summary**

36 Coastal Louisiana is affected by the combination of sea level rise and ground surface sinking, or
37 subsidence. The contribution of subsidence due to natural and human activities varies in time and
38 space. We used airborne LiDAR and SAR satellite data to estimate rates and spatial variations of
39 vertical and horizontal surface motions between 1999 and 2020 in the metropolitan area of Baton
40 Rouge where two faults with surface topography cross the region in a pattern like tilted dominos.
41 We found that the entire area is experiencing subsidence, but that the subsidence rate is faster in
42 the northern fault block than in the southern block of the study area, this pattern is opposite to the
43 long-term fault motion. The spatial pattern of the results from LiDAR and SAR data are similar
44 and relate to groundwater pumping in areas of fast subsidence and wastewater injection zones in
45 areas of slow subsidence. Our results should be considered for future urban planning and water
46 management.

47

48 **Main Abbreviations**

49 Baton Rouge Fault (BRF); Denham Springs Fault (DSF); Digital elevation model (DEM); Gulf
50 of Mexico (GOM); Interferometric Synthetic Aperture Radar (InSAR); Iterative Closest point
51 (ICP); Light Detection and Ranging (LiDAR); Line of Sight (LOS); Margin of Error (MOE);
52 Persistent Scatter Interferometry (PSI); Relative sea-level (RSL); Root Mean Square Error
53 (RMSE); Sea Level (SL).

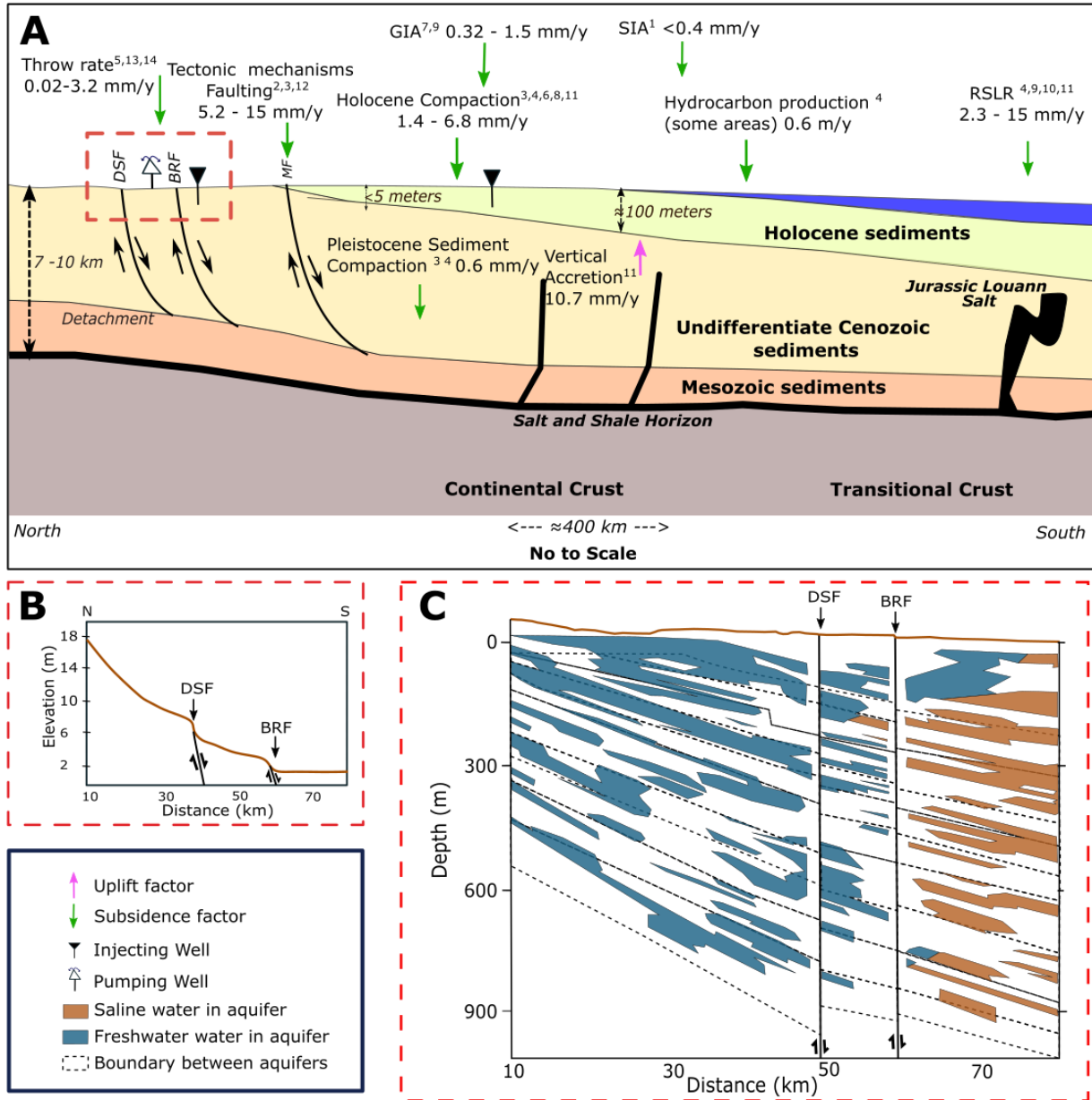
54

55 **1 Introduction**

56 Sea level (SL) rise caused by the combined effects of ice sheet melting and water column
57 expansion owing to increases in ocean temperature will affect at least 190 million people
58 worldwide living mainly in coastal areas (Milliman and Haq, 1996; Kulp and Strauss, 2019;

59 Frederikse et al., 2020). At regional scales, as in the Gulf of Mexico (GOM), thermal expansion
60 contributes greatly to SL changes (Frederikse et al., 2020). During the 20th century, global SL
61 increased between 12-15 cm (Milliman and Haq, 1996), and it is expected to rise 65 ± 12 cm by
62 2100 (Church et al., 2013; Nerem et al., 2018). The rate of SL rise in the GOM region is
63 accelerating owing to a combination of oceanographic effects (Dangendorf et al., 2023).

64 Relative sea-level (RSL) is the sum of sea-level rise and vertical crustal motions caused
65 by natural and anthropogenic processes such as fluid extraction, compaction of recent sediments,
66 isostatic adjustments, salt movement, and growth faulting (NASEM, 2018) (Fig. 1). Previous
67 estimates of RSL rate along the Louisiana coast range between 1.38 – 13.2 mm/y; variations
68 between studies depend on methods and local factors (e.g., Penland and Ramsey, 1990;
69 Pendleton et al., 2010; Karegar et al., 2015; Jankowski et al., 2017). Quantifying the different
70 processes using only one method is not an easy task (e.g., Karegar et al., 2020), and all the
71 measurements from different methods should be in the same reference frame (e.g., Shirzaei et al.,
72 2021). Considerable work has been done to quantify rates of sediment compaction in southern
73 Louisiana using Rod Surface Elevation Table horizon markers (e.g., Jankowski et al., 2017;
74 Nienhuis et al., 2017). Quantification of Glacial Isostatic Adjustment (GIA) and anthropogenic
75 contributions lack adequate spatial distribution of GNSS receivers anchored in compacted
76 sedimentary strata across the region (e.g., Dokka 2006; Pendleton et al., 2010; Keogh and
77 Tornqvist, 2019; Karegar et al., 2020). Interferometric Synthetic Aperture Radar (InSAR) offers
78 excellent spatial resolution of vertical crustal movements, and earlier studies in the GOM have
79 detected local and regional variations using individual interferograms and time series (e.g., Jones
80 et al., 2016; Fiaschi and Wdowinski, 2020). Another method consists of using Light Detection
81 and Ranging (LiDAR) data from two different surveys to perform differential LiDAR (e.g.,
82 Nissen et al., 2012; Scott et al., 2018; Wheaton et al., 2010). Recently, Zhong et al., (2022) used
83 these two tools in coastal Texas and concluded that the high spatial resolution of LiDAR can
84 improve the results from InSAR time series. InSAR and LiDAR have a good spatial resolution,
85 but the temporal resolution is lower compared to other tools such as GNSS. Integrating all three
86 tools in one area is needed to unravel the causes and spatial variability of vertical crustal
87 movements is critical to mitigation and adaptation programs along the GOM.

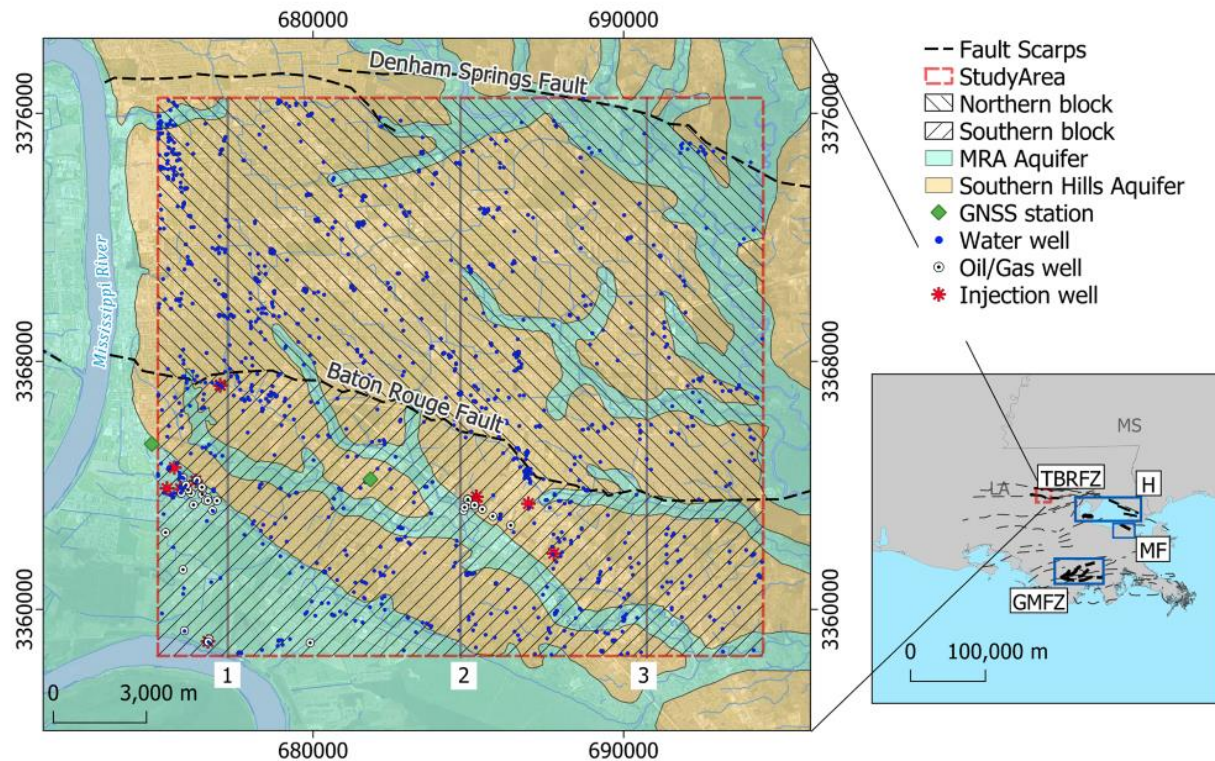


88
89 **Figure 1: A)** Schematic model of the extensional-contractional complex in southern Louisiana. Faults included in
90 the figure: Baton Rouge Fault (BRF), Denham Springs Fault (DSF), Golden Meadow Fault Zone (GMFZ), Michoud
91 Fault (MF). Study area enclosed in red rectangle. Modified from Shen et al. (2017). **B)** Topographic profile of the
92 study area. Modified from Gasparini et al., (2015). **C)** Hydrogeological setting under the study area enclosed in (A).
93 Aquifer boundaries are an approximation for the lithologic, hydrogeologic, and aquifer system contacts. The top one
94 is the 400-ft sand and the bottom one is the 2800-ft (122 m and 853 m respectively) sand, after White (2017).
95 Subsidence and uplift rates from: Kuchar et al. (2018)¹, Dokka et al. (2006)², Dokka, (2006)³, Chan et al. (2007)⁴,
96 Shen et al. (2017)⁵, Keogh and Törnqvist (2019)⁶, Love et al. (2016)⁷, Karegar et al. (2020)⁸, Karegar et al. (2017)⁹,
97 Penland and Ramsey (1990)¹⁰, Jankowski et al. (2017)¹¹, Jones et al. (2016)¹², Penland et al. (2001)¹³, Hopkins et al.
98 (2021)¹⁴.

99 The Baton Rouge region east of the Mississippi River in southern Louisiana is crossed by
100 several E-W striking growth faults that have topographic relief of ~ 5 m, with Quaternary slip
101 rates of < 1 mm/y (Shen et al., 2017)(Figs. 1, 2, 3). Hopkins et al. (2021) measured deformation

102 of man-made structures of known age in the Baton Rouge-Lake Pontchartrain region to estimate
103 fault slip rates of ~3 mm/y. These rates are 10 times faster than time-averaged rates from Shen et
104 al. (2017) (Fig. 1). The faults cut compacted Pleistocene strata reducing the number of variables
105 contributing to ground subsidence. The study of Hopkins et al. (2021) indicates that fault slip
106 rates are within the range of detection of both LiDAR and InSAR.

107 Here we use LiDAR and SAR data spanning 1999-2020 to answer the following
108 questions for the Denham Springs Fault (DSF) and the Baton Rouge Faults (BRF) (Figs. 1, 3): 1)
109 Are subsidence rates caused by fault slip significant and measurable using one or both LiDAR
110 and SAR? 2) What areas are affected by fault-controlled subsidence in the Baton Rouge area? 3)
111 Do patterns of vertical crustal movements correlate with fluid extraction and/or urban
112 development? Answering these questions will enable us to verify or refute the following
113 hypotheses: Differencing LiDAR surveys of different periods can detect small vertical motion
114 signal with enough resolution to produce similar results to InSAR; and the BRF and DSF faults
115 are slipping locally due to anthropogenic activities or by natural causes, or a mix of both. *We*
116 *chose East Baton Rouge as a test study area because there are two growth faults displacing*
117 *Pleistocene sediments where Holocene sediment compaction is small, enabling us to isolate the*
118 *signals of fault creep and anthropogenic change (Figs. 1, 2).* We use information from two
119 continuous GNSS stations processed by the Nevada Geodetic Laboratory (Blewitt et al., 2018) as
120 control points in LiDAR and InSAR data sets. We also compare the results with well data from
121 the Louisiana Department of Natural Resources (SONRIS, n.d.) to investigate whether there is a
122 spatial correlation between fault slip and injection and extraction well volumes and rates over the
123 last two decades.



124
 125 **Figure 2:** Baton Rouge study area with respect to the Gulf of Mexico margin in Louisiana showing GNSS sites,
 126 water and oil/gas extraction wells and injection wells. The Denham Springs (DSF) and Baton Rouge (BRF) are
 127 growth faults with Holocene slip (Shen et al., 2017). The Northern block lies between the DSF and BRF; the
 128 Southern block is the hanging wall of the BRF. Inset shows the location of the study area with respect to the
 129 Mississippi delta, surrounding states, and main fault systems in Louisiana. Michoud fault (MF), Golden Meadow
 130 fault zone (GMFZ) and the faults used by Hopkins et al. (2021) (H) are shown. MRA is Mississippi River Alluvial
 131 Aquifer. Fault scarps from Culpepper et al. (2019b). Well data and aquifers from the Louisiana Department of
 132 Natural Resources (SONRIS), (n.d.). GNSS stations from the National Geodetic Survey (n.d.). Gray vertical lines
 133 and numbers are profiles for Figure S1. Base map imagery from QuickMapServices - QGIS (Map data ©2015
 134 Google).

135 1.1 Background

136 The GOM is a passive margin that formed between 200-158 Ma during the breakup of
 137 Pangea, resulting in pervasive, general E-W-striking normal fault systems bounding 3-10 km-
 138 deep sedimentary basins (e.g., Sawyer et al., 1991; Pindell and Kennan, 2009; Eddy et al., 2014).
 139 Mesozoic growth faults in the Mississippi delta are listric faults that detach on salt horizons
 140 (Durham and Peeples, 1956; Culpepper et al., 2019). These faults accommodated extension until
 141 ~40 Ma, but much slower movement associated with compaction and salt migration has
 142 continued to present day (Shen et al., 2017). Despite the ~5 m fault scarps (Fig. 3) and evidence
 143 for ongoing movement, there are only three instrumentally recorded earthquakes of M2.4-3.8
 144 along the coastal fault systems of Louisiana (Stevenson and Agnew, 1988; Walter et al., 2016),
 145 suggesting that slip occurs primarily by creep.

146 The GOM is characterized by its low elevation coasts, broad continental shelf, steep
147 continental slope, and a basin as deep as 4400 meters (e.g., Turner and Rabalais, 2018). The
148 Mississippi River flows into the GOM, through the Mississippi delta. The delta began to develop
149 at ~100 Ma with the formation of the Mississippi embayment, which concentrated sediment
150 input to the gulf. During the last 7000 years, the delta depocenter relocated at least six times in
151 response to climate and sea-level changes (Blum and Roberts, 2012). In the last 100 years, the
152 Mississippi delta has suffered drastic land loss (Gagliano et al., 1981). This could lead to a shift
153 of the depocenter of the Mississippi delta caused by sea-level rise, climate change, anthropogenic
154 activities, and the lack of sediment delivery caused by artificial dams (e.g., Blum and Roberts,
155 2012). Glacial Isostatic Adjustment (GIA) and Sediment Isostatic Adjustment (SIA) contribute to
156 long-term subsidence (e.g., Kuchar et al., 2018). GIA was modeled using RSL data from tide
157 gauges and vertical and horizontal velocities from GNSS between 2006-2015 along the GOM by
158 Love et al. (2016). During this century GIA in southeast Louisiana will contribute approximately
159 30 mm to RSL rise with a rate of 0.32 mm/y (Love et al., 2016). On the other hand, SIA registers
160 a rate of less than 0.5 mm/y on areas with thicker Holocene sediments (Wolstencroft et al., 2014;
161 Kuchar et al., 2018).

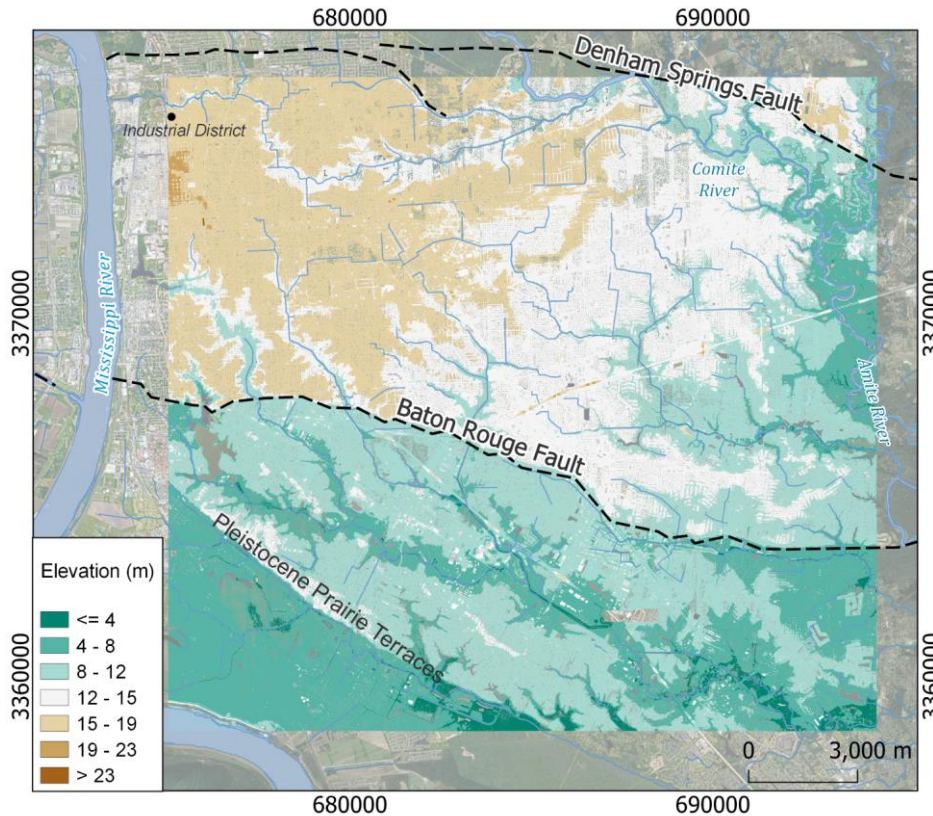
162 Holocene sediment thickness increases following the shape of the Mississippi river,
163 reaching a thickness of 100 meters at the shoreline (Penland and Ramsey, 1990). Compaction
164 and compression of Holocene sediments are the primary factors causing subsidence on the
165 Mississippi delta in areas close to the shoreline (e.g., Penland and Ramsey, 1990; Karegar et al.,
166 2015; Karegar et al., 2020). Shallow subsidence in the uppermost 5 meters in the Mississippi
167 delta accounts for more than 60% of the total subsidence in the coastal area with rates varying
168 between 6.4 ± 5.4 and 9 ± 1 mm/y (Keogh and Törnqvist, 2019; Jankowski et al., 2017; Nienhuis et
169 al., 2017).

170 Despite the importance to infrastructure, there are just a few studies that have quantified
171 fault slip rates and their relationship with subsidence at different time scales in the area, with
172 rates ranging between 0.02 – 16.9 mm/y (Gagliano et al., 2003a, 2003b; Dokka et al., 2006; Shen
173 et al., 2017; Culpepper et al., 2019a; Hopkins et al., 2021). Fault slip and creep are difficult to
174 quantify because they can be episodic and slow, and the signal can be masked by faster processes
175 such as sedimentation (Gagliano et al., 2003b). Salt movement may reactivate some fault
176 segments (Gagliano et al., 2003a). Local subsidence has been related to the presence of fault

177 traces and fluid extraction sites (e.g., Kuecher et al, 2001; Morton et al, 2002; Dokka, 2011).
178 Dokka (2006) and Dokka et al., (2006) interpreted episodes of subsidence along the Michoud
179 fault (MF) between 1955 to 2005 as evidence of episodic fault slip, although they could also be
180 caused by groundwater extraction (Jones et al., 2016). Fault motion and subsidence near the
181 Golden Meadow fault zone (GMFZ) have been related to hydrocarbon extraction (e.g., Morton et
182 al., 2002; Chan and Zoback, 2007).

183 There is visual evidence of building and road displacements along the BRF and other
184 coastal faults with measured rate estimates of ~3 mm/y (McCulloh, 2001; Hopkins et al., 2021).
185 The BRF and DSF reactivated during the Pleistocene due to depositional loading (McCulloh and
186 Heinrich, 2013). Shen et al. (2017) calculated mean fault throw rates in the eastern portion of the
187 BRF using optically stimulated luminescence dating. Their results indicate that the faults have an
188 average slip of 0.22 mm/y for the past 4,000 years and between 0.02-0.07 mm/y for the last
189 130,000 years for areas lying on Pleistocene sites. The relief caused by Pleistocene-Recent slip
190 along the BRF is clear in DEMs produced from LiDAR data (Fig. 3). Faults in this system merge
191 at a depth of ~6 kilometers into a detachment that sits on an overpressured layer of salt and shale
192 that dips with an angle between 45° to 65° (Gagliano et al., 2003a; Shen et al., 2017) (e.g., Figs.
193 1).

194 Local subsidence has been related to the presence of fault traces and fluid extraction sites
195 (e.g., Kuecher et al, 2001; Morton et al, 2002; Dokka, 2011). Wells in Baton Rouge have
196 multiple purposes like water, gas and oil withdrawal, water injection and monitoring, with depths
197 ranging between 4-6000 meters. The change of pore fluid pressure underground caused by fluid
198 extraction/injection changes the volume at depth, which could influence fault activation (e.g.,
199 Kuecher et al., 2001). Multiple studies have related extraction of fluids with local subsidence at
200 different locations (e.g., Jones et al., 2016; Puskas et al., 2017; Li et al., 2020), and uplift with
201 injection of fluids (Teatini et al., 2011; Shirzaei et al., 2016).



202
 203 **Figure 3:** Digital Elevation Model from the study area showing the topographic relief across the Denham Springs
 204 and East Baton Rouge faults (dashed lines). The geological contact labeled as Pleistocene Prairie Terraces marks the
 205 edge of the natural levee in the area. We created this DEM using LiDAR point cloud from the 2018 survey. Base
 206 map imagery from QuickMapServices - QGIS (Map data ©2015 Google).

207 The aquifer system in Baton Rouge is part of the Southern Hills aquifer and the
 208 Mississippi River Alluvial aquifer (Tomaszewski et al., 2002) (Fig. 2). The former is composed
 209 of interbedded layers of compressed clay/silt and layers of porous sands (Fig. 1). The sands south
 210 of the BRF are more continuous than those north of the fault (Vahdat-Aboueshagh and Tsai,
 211 2021). These sands form ten independent aquifers named after their depth under the Baton
 212 Rouge industrial district, with depths between 122 to 823m (400 ft to 2700-ft) (Tomaszewski et
 213 al., 2002). Large volumes of groundwater removal have affected reservoirs in the Baton Rouge
 214 area forming cones of depression at local and regional scales (White, 2017; Chen et al., 2023),
 215 and saline water from southern areas has intruded into some of these sands (Nasreen, 2003;
 216 Elshall et al., 2013). Similarly, other areas in Louisiana have shown saline intrusion in areas of
 217 fault motion (e.g., Kuecher et al., 2001). Deep aquifers have larger withdrawal volumes, and,
 218 therefore, have been more affected during the last decades (Tomaszewski et al., 2002; Nasreen,
 219 2003). The Mississippi River Alluvial aquifer has not had a significant groundwater level

220 decrease, and saline water has not infiltrated the eastern portion of the aquifer where the study
221 area is located (Tomaszewski et al., 2002; Nasreen, 2003; Chen et al., 2023).

222 The BRF plays an important role in the dynamics of the aquifers in Baton Rouge; it is a
223 barrier for saline water coming from the southern area, but it may serve as a conduit and can
224 allow lateral intrusions due to pumping of groundwater at the north of the fault (Nasreen, 2003;
225 Elshall et al., 2013; Anderson et al., 2013; Chen et al., 2023). The DSF is permeable and allows
226 freshwater to flow down to the south, where pressure gradients cause southward flow and
227 recharge to the aquifers in the area between the two faults (Elshall et al., 2013).

228 **2 Data**

229 **2.1 SAR data**

230 SAR datasets were acquired by the EnviSAT and Sentinel-1 satellites. Both acquire data
231 on the C-band (5.405 cm) and produce Single-Look Complex images. We used vertical transmit
232 and receive polarization (VV). The EnviSAT dataset was collected between 2004 and 2010 in
233 the relative orbit 83 and it is composed of 18 scenes (ESA, 2021a) in descending mode. The
234 Sentinel-1 dataset was collected in Interferometric Wide mode between 2017 and 2020 and
235 consists of 33 scenes all acquired in the relative orbit 165 (ESA, 2021b) in ascending mode. Each
236 of these datasets forms a different time series that was analyzed separately. The list and dates of
237 images is in Table S1.

238 **2.2 LiDAR data**

239 LiDAR point clouds come from two surveys that cover the portion of the BRF and DSF,
240 East Baton Rouge parish. The first dataset was collected in March of 1999, has a point space of 4
241 m (0.0625 points/m²), a pulse rate of 15 kHz and a vertical accuracy measured as the Root Mean
242 Square Error (RMSE) of 15 cm (USACE, 2001). The newest was collected between March and
243 April of 2018, has a point space of 0.33 m (9.2 points/m²), a pulse rate of 450 kHz and a vertical
244 accuracy of RMSE=3.6 cm (USGS, 2019). For more details see Table S2.

245 **2.3 Well data**

246 Data about injection and extraction of fluids from the wells comes from the Louisiana
247 Department of Natural Resources website. The wells included here are those that were active
248 between 1999 and 2020 or for a shorter time in that period and were in the database by August

249 2021. For wells extracting water, we only used active wells whose main function was water
 250 pumping. In the case of wells producing oil and gas, we only considered those with gas
 251 production of at least 200,000 MCF or produced more than 20,000 m³ of oil during the study
 252 period (Fig. S4). Not all the wells have complete information about volume of production or
 253 injection, but if they appeared as active, we included those for location information in our maps.
 254 Table 1 summarizes the number of wells found and used. However, wells that were operating
 255 before can, in some cases, caused delayed pore pressure changes and deform the surface
 256 (Shirzaei et al., 2016).

257

258 **Table 1:** Number of wells in the study area per fluid. This table excludes 1908 wells that are used to monitor water
 259 level and quality.

	Water	Oil – gas	Injection
Total wells in area	821	368	24
Current active wells (By august/2021)	470	6	2
Active wells between 1999 -2021	592	47	13
Wells with volume extraction/ injection information		23	9

260

261 **2.4 GNSS time series**

262 There are two continuous GNSS stations in the study area (Fig. 2). Both stations are
 263 mounted on buildings and there is no public information about the foundation depth for any of
 264 the stations. The ILSU station worked between 2004-2022 and it is mounted on the Patrick F.
 265 Taylor Hall building, constructed on the Mississippi River Alluvial Aquifer (Fig. 2) and the
 266 Pleistocene Terraces (Fig. 3). The local geology makes the ILSU site sensitive to hydrological
 267 changes of the Mississippi River as compared to the SJB1 station. The SJB1 station has acquired
 268 data between 2009-2023 and it is mounted on the LifeShare Blood Center constructed above the
 269 Southern Hills aquifer which lies at deeper depths than the Mississippi River Alluvial Aquifer
 270 and does not have direct contact with any water body (Fig. 2). North, east, and up velocities of
 271 the GNSS stations are calculated by the Nevada Geodetic Laboratory (Blewitt et al., 2018).
 272 Vertical time series for both stations are in Fig. S3.

273 **3 Methods**

274 **3.1 Persistent Scatter Interferometry - PSI (time series InSAR)**

275 PSI is a differential InSAR technique that allows one to use the phase information from
276 multiple SAR images acquired at different times to estimate phase changes between several
277 interferograms. Phase change information is used to calculate the velocity of displacement and
278 the displacement time-series during the study period (Hooper et al., 2004; Crosetto et al., 2016).
279 PSI uses pixels with low phase noise, called Persistent Scatterers (PS), across lengthy time
280 intervals in multi-temporal data. It is particularly useful in urban areas that have a high density of
281 persistent, or permanent, scatterers (Ferretti et al. 2001; Crosetto et al., 2016). Displacement is
282 calculated on the Line of Sight (LOS), projecting 3D displacements into 1D displacements in the
283 LOS direction (Crosetto et al., 2016). One of the advantages of this technique is its ability to
284 detect signals of ground displacement at millimetric scales with an accuracy of millimeters
285 depending on the number of images in the time series, the density of PS, temporal baseline
286 dispersion, and terrain conditions (Ferretti et al., 2001; 2004; 2007).

287 A description of this technique is found in the official manuals (L3Harris, 2014; 2021),
288 Ferretti et al., 2001, and in the Supplemental material (T1). We used SARscape software (version
289 5.6; 2021) to calculate vertical displacement velocity for both datasets. The topographic phase
290 was removed using the Shuttle Radar Topography Mission DEM. Orbital errors can be ~0.5
291 mm/y/100 km for EnviSAT and ~0.2mm/y/100 km for Sentinel-1 in the LOS direction (Fattahi
292 and Amelung, 2014), but effectively cancel for InSAR time series with several images as the
293 ones presented here. Ionospheric errors are negligible because we are using data captured on the
294 C-band and the study area is at midlatitude where ionospheric corrections are not recommended
295 (Liang et al., 2019). Tropospheric phases are estimated from the residuals from the linear model
296 calculated by SARscape (Ferretti et al., 2001; Supplemental material - T1). To provide a
297 numerical approximation of the tropospheric variation over the study area during the study
298 period we present an empirical analysis using GACOS data (Yu, et al. 2017; Supplemental
299 material – T2). For the EnviSAT time series (2004-2010) the average range of the tropospheric
300 delay is 28.75 mm and for Sentinel-1 time series (2017-2020) it is 35.95 mm.

301 We multilooked the data to reduce decorrelation noise and build the spatial coherence
302 map (Goldstein et al., 1988; Fig. S5). For the EnviSAT dataset we used four azimuth-looks and
303 one range-look; for the Sentinel-1 dataset we used five azimuth-looks and one range-look. The

304 entire area is divided into sub-areas, each is 25 km² and every subarea is independently
305 processed. By default, just one reference point is selected for each subarea. Reference points
306 were selected using an Amplitude Dispersion Index >60%. A 30% overlap of subareas is used in
307 the mosaicking process to merge all the sub-area results. The merging process is carried out
308 considering a Super Reference Point (Fig. 4 and 5) which is characterized by the highest
309 Amplitude Dispersion Index among the others. Coherence used for merging all sub-areas is 0.77.

310 **3.2 LiDAR pre co-registration**

311 Co-registration of the LiDAR point clouds is the process of aligning datasets acquired at
312 different times over the same area. It is important to know the magnitude and the direction of the
313 horizontal misalignment to correct the geographical location of the point clouds to improve
314 vertical differencing between corresponding points. This process reduces systematic errors
315 (Anderson, 2019). Misalignments between the point clouds can be caused by 1) distortion of the
316 point clouds from measurement errors related to flight discrepancies; 2) real changes in the
317 landscape (subsidence, uplift, translation, vegetation growth, mass movement); and 3) local
318 topographic relief on flat surfaces where there is less random LiDAR scattering (Scott et al.,
319 2018).

320 We conducted point cloud co-registration using ICP (Section 3.3) in two ways: using
321 only LiDAR ground points and using LiDAR points from structures that should be stable over
322 time and are anchored to some foundation depth (e.g., Fig. S2). For the first approach, ground
323 points were taken using the original classification of both point clouds done by the distributors.
324 For the second approach, a feature-based technique allows us to take information from structures
325 that are expected to be stable and use them as control points (Brook and Ben-Dor, 2011). Using
326 Point Data Abstraction Library (2018) filters (PDAL), we created a new point cloud for each
327 dataset whose points only belong to structures that satisfy specific criteria. First, the point must
328 be on a plane. To evaluate this criterion, we used the filter “estimatorank”, which categorizes
329 each LiDAR point in a line, plane, or a 3D structure. Secondly, the points must be in an elevation
330 range assigned depending on if they are in the hanging wall or footwall of the BRF. The range
331 for the hanging wall is 7 m to 35 m and for the footwall is 12 m to 35 m. These values were
332 chosen from observation of the LiDAR data, using the maximum value from tall buildings and
333 the lowest from roads and parking lots. DEMs show that there are at least ~5 m of relief along
334 the BRF (Fig. 3); therefore, features on the hanging wall are expected to be at a lower elevation.

335 We allowed for North and East movements of the 2018 (newest) point cloud to co-
 336 register the 1999- and 2018-point clouds. The translation amount was estimated by ICP. We
 337 calculated the average motion in the east and north components for areas of 2.25 km². This
 338 process ensures that vertical DEM differencing is more accurate. We did this process with
 339 ground LiDAR points and LiDAR points from stable structures.

340 **3.3 Iterative Closest point – ICP**

341 This algorithm allows one to perform 3D LiDAR differencing by calculating rotations
 342 and translations of a surface (Scott et al., 2018; Nissen et. al., 2012). The ICP algorithm aligns
 343 the point clouds using user-defined core points in the two datasets. Each core point is defined by
 344 a grid of 50 m and centered in a square or window of 50x50 m in the 1999-point cloud and
 345 51x51 m in the 2018-point cloud. We chose these values for computational optimization. The
 346 horizontal coordinates of each core are the central point in each window. ICP assumes that each
 347 window behaves as a rigid body (Nissen et. al., 2012).

348 This algorithm iterates as follows for each window: 1) Find the closest point in the old
 349 point cloud for each point in the new point cloud, 2) Calculate translation and rotation of each
 350 point in the old point cloud, 3) Iterate until a minimum distance is reached or until a certain
 351 number of iterations are completed (Scott et al., 2018; Nissen et. al., 2012). We iterated until the
 352 translation was less than 10⁻⁴ meters or when 10 iterations were completed. ICP applies a linear
 353 transformation to the old data to have the best alignment possible. It finds the rigid body
 354 transformation matrix, with α , β and γ representing the rotations on the x, y, and z axes, and t_x ,
 355 t_y , t_z representing the translations in the same three axes in equation 1 (Scott et al., 2018).

$$356 \quad PC_{new} \approx PC_{old\ transformed} = \begin{pmatrix} 1 & -\gamma & \beta & t_x \\ \gamma & 1 & -\alpha & t_y \\ -\beta & \alpha & 1 & t_z \\ 0 & 0 & 0 & 1 \end{pmatrix} PC_{old} \quad (Eq. 1)$$

357 Where PC_{new} is the newest LiDAR point cloud, in this case the one from 2018, PC_{old} is the
 358 original and oldest LiDAR point cloud, here corresponding to the one from 1999, and
 359 $PC_{old\ transformed}$ is the transformed old LiDAR point cloud. We run the ICP algorithm with LiDAR
 360 ground points and with LiDAR points from stable surfaces chosen in the co-registration section.
 361 In both cases, ~122,400 core points and windows were created. The windows do not have the
 362 same number of LiDAR points. The results of this ICP implementation provide the amount of

363 translation that must be applied to each window in the newest point cloud to align the dataset
364 with the oldest point cloud. The translations of each window are represented on each core point.

365 These results were filtered to have only displacements between 0 to 1 m to eliminate
366 outliers (e.g., new constructions), and not natural displacements. Then, results were averaged to
367 have a representative point per 2.25 km². The error for this process is given initially by the Point-
368 to-Plane error metric (Scott et al., 2018; Nissen et. al., 2012), and the final averaged results were
369 evaluated using a 95% margin of error and the residual systematic error described on section 3.5.
370 We use the 3D_Differencing MATLAB code created by Scott et al. (2020) to apply ICP to
371 LiDAR data, which uses the LIBICP (LIBrary for Iterative Closest Point fitting) software created
372 by Geiger et al. (2012) to solve the rigid body transformation. The horizontal translations
373 calculated by ICP are used to co-register the datasets (Section 3.2), but these displacements can
374 include real motion. We discuss the real part of this motion in the results and discussion sections.

375 **3.4 Vertical DEM differencing**

376 Vertical differencing between the two data sets is achieved using Geomorphic Change
377 Detection (GCD) software. It allows one to detect topographic and volumetric changes using
378 digital elevation models (DEM) (Wheaton et al., 2010). With GCD we created a DEM of
379 Differences doing pixel by pixel differentiation. The vertical accuracy of these is given by
380 standard error propagation and depends on the accuracy of the original point clouds (Wheaton,
381 2018). We created the DEMs using PDAL filters to include only co-registered ground LiDAR
382 points. We used Inverse Distance Weighting with PDAL tools to interpolate the data (Shepard,
383 1968). We used a pixel size of 5 m, and a radius of 5 m for the 1999-point cloud and 3 m for the
384 2018-point cloud. The radius is different to ensure that the DEMs from 1999 have enough points
385 to interpolate. We used a power parameter equal to 2 because it has been shown to produce good
386 empirical results and it is computationally efficient (Shepard, 1968). The error of each DEM with
387 respect to the original LiDAR data was estimated using the root mean square error metric. Figure
388 S10 shows the workflow followed to process the LiDAR data.

389 **3.5. Error estimation**

390 Systematic errors can impact the estimated changes from LiDAR. As we co-registered
391 the data, it is expected that systematic errors caused by flight discrepancies are reduced but not
392 completely removed (e.g., Anderson, 2019). This error type can dominate the error budget in the

393 analysis of vertical ground changes (e.g., Anderson, 2019). We assume a residual systematic
394 error from the LiDAR results (Fig. 7A and 7B) of 44.8 mm (2.3 mm/y). This number is the
395 difference between the results of ground and stable surfaces on the fourth row from Figure 7A
396 and 7B where an E-W stripe appears. The systematic problems are probably E-W flight line
397 errors.

398 We present uncorrelated random errors as the Margin of error (MOE) of the Mean. It is
399 calculated as $MOE_m = z \times \frac{\sigma}{\sqrt{n}}$. Where $z = 1.96$ corresponds to a confidence level of 95% for the
400 average mean, σ is the sample standard deviation of the mean averaged points, and n the sample
401 size. We used this metric to quantify the random component of the error due to the different
402 areas for each sampling (2.25 km² and for each block of the fault ~175 km²), but not for
403 individual points. The total uncertainties should include the RSE to better bound the results.
404 In the case of LiDAR, we are aware that each survey has an associated RMSE estimated by the
405 distributor (Section 2.2). The RMSE quantifies the discrepancy between the location of
406 checkpoints and the Triangulated Irregular Network generated from the point clouds by the
407 distributors (USACE, 2001; USGS, 2019). Then, in the worst case, each pixel on each DEM can
408 be wrong by 15 cm and 3.6 cm in the vertical component, if each pixel in each DEM only
409 contains one LiDAR point from each survey, and the vertical change in each pixel could have an
410 error of 15.43 cm. This extreme case is not a concern owing to our approach of comparing areas
411 from each survey and not individual pixels. For instance, each ICP - LiDAR window of 50 m
412 may have ~100 LiDAR points in each point cloud. Using the results of displacement for each
413 window (Section 3.3) we found the mean vertical displacement for 2.25 km² areas, then we
414 calculated the corresponding MOE with the number of windows (~1000) as the sample size. For
415 InSAR time series we present MOE using the total number of PS points for each block as the
416 sample size. Systematic errors for InSAR time series were corrected during the PSI processing
417 and their ranges are described (Section 3.1 and Supplemental material – T1).

418

419 **3.6. Tie of Results**

420 We used the ILSU station as a tie point for all the results but EnviSAT and SJB1 as a
421 control point to compare the results after this connection. We selected ILSU because it has the
422 longest time series between the two stations. The results from the three geodetic tools (GNSS,
423 InSAR time series, and LiDAR differencing) are in different reference frames, so we

424 transformed the GNSS velocities (with plate fixed) from ITRF2014 to NAD83 using the online
425 application Horizontal Time-Dependent Positioning from NOAA (Pearson and Snay, 2013).

426 To tie the results, we calculated the difference between the displacement of 1LSU and the
427 results from LiDAR and InSAR time series in the location of the station. Then, that difference is
428 added/subtracted from each dataset to match the results with the results of the 1LSU station in
429 that location, such that all the results are referred to the same point (Mahatra et al., 2018). The
430 InSAR time series were tied to 1LSU by projecting to the LOS displacements of the station using
431 the incidence and heading angle for each dataset. For ICP, the tie with 1LSU was done in the
432 three components, and for LiDAR differencing it was done only in the vertical component. Due
433 to this process, the original results are moved by a constant, and this process does not change the
434 errors.

435 **4 Results**

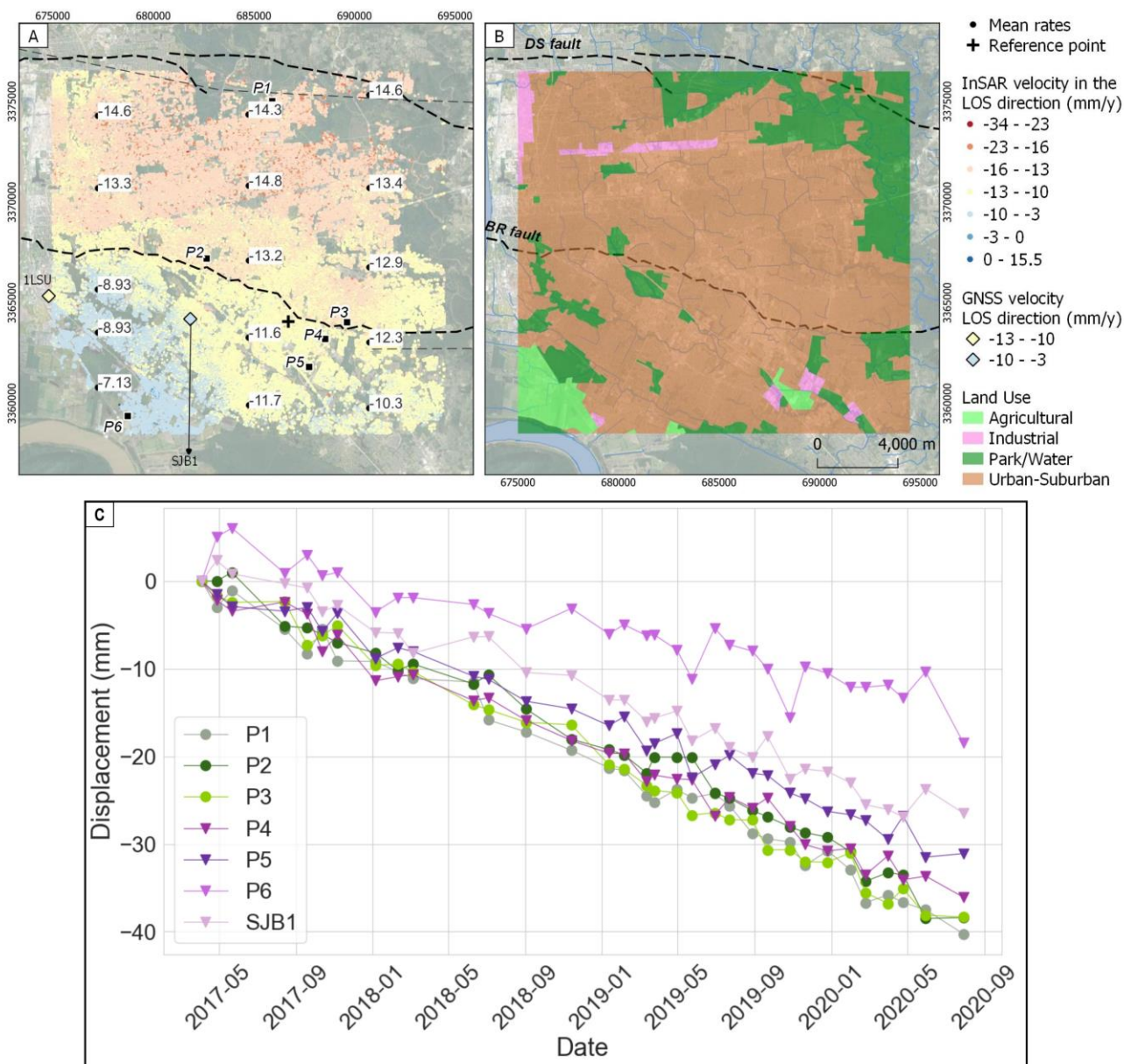
436 **4.1 Velocities from InSAR time series – Envisat and Sentinel-1**

437 The results of the InSAR time series created with Sentinel-1 data do not show results for
438 the footwall of the DSF (Fig. 4) and the results from EnviSAT are very noisy to interpret (Fig.
439 5). The area covered by our study area at the north of the DSF is mostly covered by vegetation,
440 so there is high decorrelation and there are not enough persistent scatterers (Fig. 4B). We
441 therefore focus on the BRF.

442 For the case of discussion, we call the footwall block of the BRF the northern block and
443 the hanging wall of the BRF the southern block as indicated in Figure 2. After removing the
444 difference of motion with the GNSS station 1LSU from the results, the InSAR time series using
445 Sentinel-1 indicates that the northern block is moving away from the satellite at a larger rate than
446 the southern block (Fig. 4A). PSI detected 411,857 persistent scatterers. Areas labeled as
447 Agricultural, or Park/Water (Fig. 4B) do not have enough persistent scatterers. Therefore, we
448 cannot produce results over these areas with PSI. The mean velocity between 2017-2020 using
449 Sentinel-1 data for the complete northern block is -13.65 ± 0.00471 mm/y while the southern
450 block has a mean velocity of -10.559 ± 0.00895 mm/y. The SJB1 station differs from the InSAR
451 time series in ~ 2.33 mm/y (Fig. 4).

452 Figure 4C shows some examples of the time series in the area. Each time series is the
453 average displacement of the persistent scatterers that are in a specific location (details in Table

454 S3). The time series of P6 shows less displacement; it is located on the Baton Rouge Wastewater
 455 Treatment plant which lies ~500 m from injection well 200837 and ~2000 m from the 136676
 456 injection well. The time series for the building where the SJB1 station is anchored and the area
 457 P5, which surrounds the injection well 189576, are the next series with less displacement. The
 458 areas identified as P2, P3, and P4 have similar displacements and are the sites closest to the
 459 BRF.

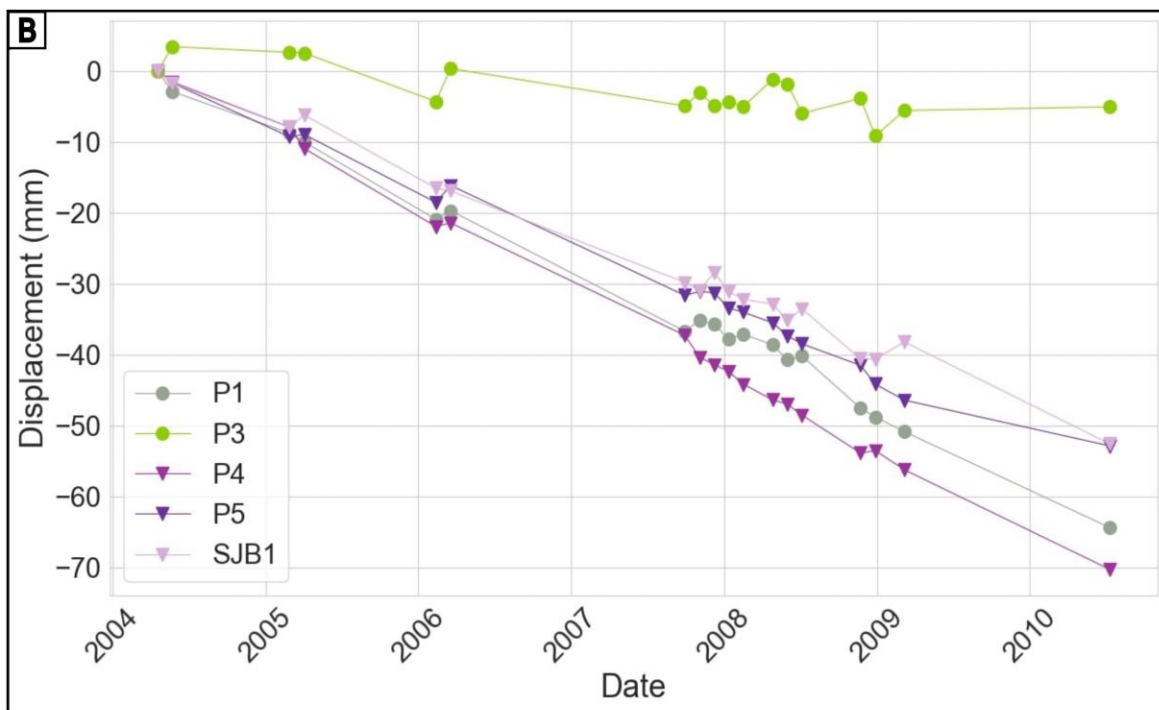
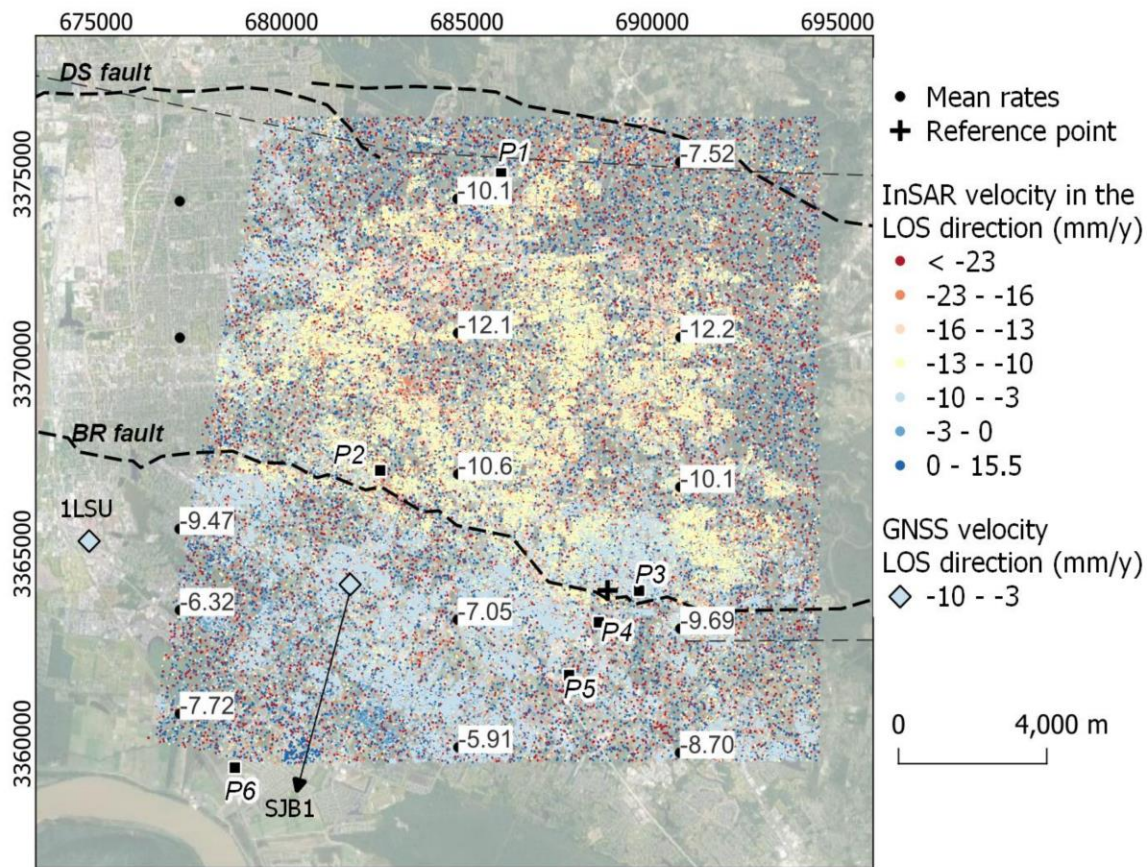


460
 461 **Figure 4:** Rates produced with Sentinel-1 (2017-2020) compared to Land use. (A) Displacement rates in the LOS
 462 direction calculated with the PSI method. These results are tied to the 1LSU GNSS station. Numeric labels in the
 463 image indicate mean rates for the black dots. The cross is the initial reference point used to create the time series.

464 Rhombuses are the average velocities of the GNSS CORS stations in the LOS direction on the Sentinel-1 geometry
465 (ILSU -10.88 mm/y and SJB1 -8.404 mm/y). **(B)** We mapped land use using the basemap imagery from
466 QuickMapServices - QGIS (Map data ©2015 Google) at a scale of 1:10,000. **(C)** Time series examples located in
467 (A); green colors show samples in the northern block and purple colors show samples in the southern block. These
468 time series are the average of the displacements of the points that landed in the same construction, with details on
469 Table S3. Displacement in the LOS direction.

470 The velocity in the LOS direction for the study area using EnviSAT data is shown in
471 Figure 5A. This dataset does not cover the 1LSU station, and it is the only one that was tied to
472 the SJB1 station. The PSI process detected 172,791 persistent scatterers. These results are noisy
473 in some areas, although it is possible to see similar patterns with the results of Sentinel-1
474 analyses. Figure 5A shows that the entire area is subsiding but the northern block is moving
475 away from the satellite faster than the southern block. The northern block is moving with a
476 velocity of -10.869 ± 0.0384 mm/y and the southern block at a rate of -8.030 ± 0.0614 mm/y. The
477 noise also can be related to land-use changes during that period after Hurricane Katrina in 2005.
478 This will be further explained in the discussion section.

479 The example time series with EnviSAT shows that the P3 area was the most stable
480 among these examples, although it is close to the reference point of the time series in this dataset.
481 Sample P3 shows a large mismatch between the Sentinel-1 and EnviSAT results (Fig. 4C and
482 5B), but this area has homes constructed in 2017, before the area showed fewer coherent
483 persistent scatterers in EnviSAT as compared to Sentinel-1 data. We suspect that the change in
484 land use contributes to differences between datasets. The other areas show a similar behavior
485 (Fig. 5B). Details about each time series are in Table S3.



486
 487 **Figure 5:** Rates produced with Envisat data (2004-2010) (A) Displacement rates in the LOS direction produced
 488 using the PSI method. These results are tied to the SJB1 GNSS station. Numeric labels in the image indicate mean
 489 rates for the black dots. The cross is the reference point used to create the time series. Rhombuses are the average

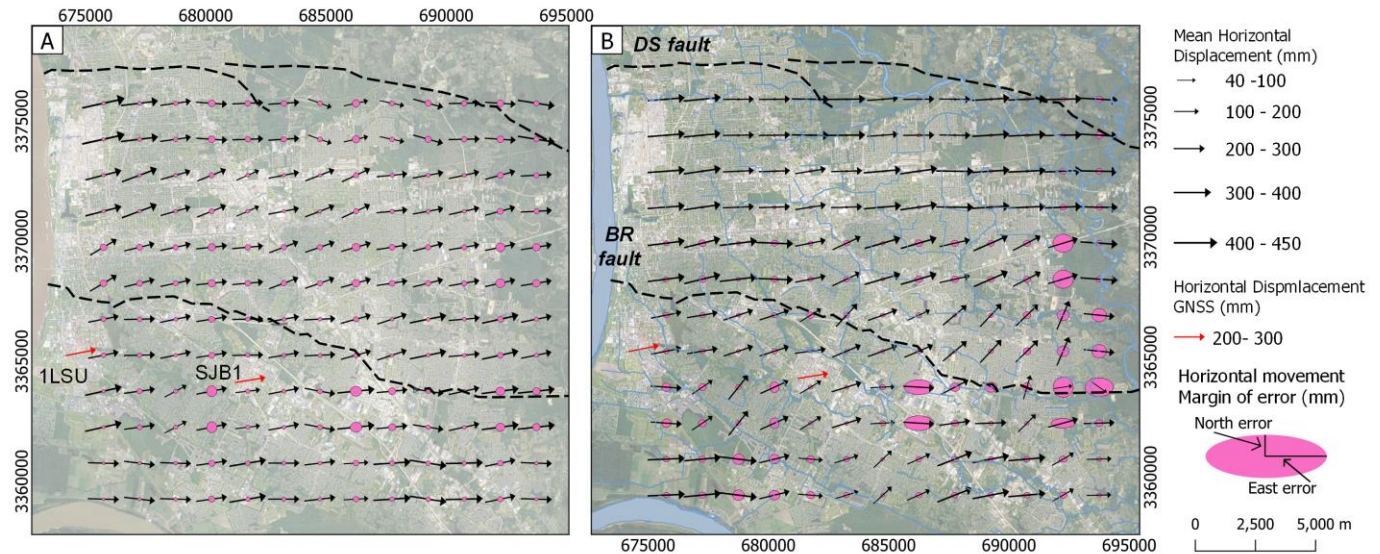
490 velocities of the GNSS CORS stations in the LOS direction on the EnvisAT geometry (ILSU -9.81 mm/y and SJB1
491 -7.23 mm/y). (B) Time series examples located in (A); green colors show samples in the northern block and purple
492 colors show samples in the southern block. These time series are the average of the displacements of the points that
493 landed in the same construction, with details on Table S3. P2 and P6 do not have a time series because the
494 construction was not in place before 2010. Displacement in the LOS direction. Base map imagery from
495 QuickMapServices - QGIS (Map data ©2015 Google).
496

497 **4.2 LiDAR Horizontal displacement from ICP**

498 The results from ICP indicate that overall, the entire area moved towards the east
499 direction between 1999-2018 in the NAD83 reference frame (Fig. 6). Results of horizontal
500 displacement created with two different LiDAR classifications – ground LiDAR points and
501 stable surface LiDAR points (Fig. 6B) – have different spatial behaviors in some areas.
502 Horizontal displacements estimated using just ground LiDAR points (Fig. 6A) are more
503 homogenous showing that the whole area moved to the east with small displacements in the
504 north component (Table 2).

505 The horizontal displacement calculated using LiDAR points on stable surfaces shows
506 more heterogenous behavior (Fig. 6B). In the north area of the northern block most areas moved
507 to the east direction, but in the southeast of the same block near the BRF, the direction is mostly
508 north-east (Table 2). These results also show that the largest errors occur in the areas closer to
509 the eastern section of the BRF. A caveat of only using LiDAR points on stable surfaces is that
510 this set of points is less dense than the set of ground points, and affected mostly by the oldest
511 LiDAR survey, which may explain why the errors are smaller in the case of only ground LiDAR
512 points.

513 Our results agree in the direction of motion with the motion of the SJB1 station (Fig. 6,
514 Table 2). The magnitude of the motion using the rates from the GNSS SJB1 station between
515 1999-2018 is 42.18 mm to the north and 260.11 mm to the east. Comparison to the results with
516 LiDAR ground points (Fig. 6A), shows almost double our estimate in the north component but a
517 difference of only 3 mm in the east component, considering the mean value of the block.
518 Comparison of SJB1 GNSS station with the results with only LiDAR points on stable surfaces
519 (Fig. 6B) shows that the north component is smaller by ~13 mm and larger in the east component
520 by ~35 mm.



521
 522 **Figure 6:** Horizontal displacements calculated with the ICP algorithm. **(A)** Horizontal displacements using ground
 523 LiDAR points. **(B)** Horizontal displacements using stable surface LiDAR points. Each black arrow represents the
 524 average displacement of an area of 2.25 km². Arrow directions represent the mean displacement direction, and the
 525 length of the arrow represents the mean displacement magnitude. Ellipses show the error multiplied by 30 for
 526 visualization, where East error represents the error in the east component and North error represents the error in the
 527 north component. Red arrows are horizontal displacements using the rates from the GNSS stations for 19 years.
 528 Base map imagery from QuickMapServices - QGIS (Map data ©2015 Google)

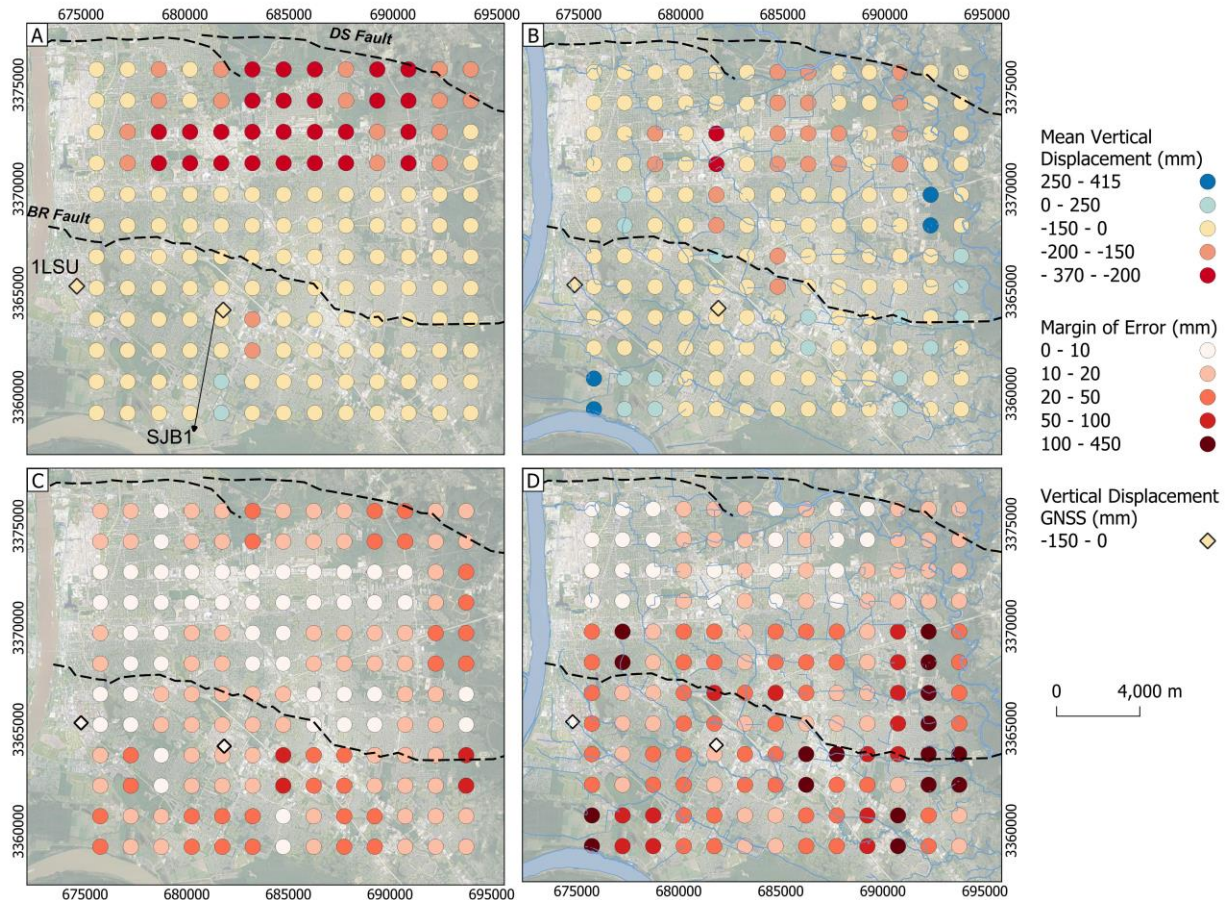
529 4.3 Vertical displacement from LiDAR

530 In this section, we show the results for vertical displacement using ICP and Vertical
 531 DEM differencing. These two methodologies give us similar results: there is subsidence across
 532 the complete region and subsidence is larger in the northern block than in the southern block.
 533 Some regions show uplift mostly in the southern block and it is localized in areas where InSAR
 534 time series have smaller rates (Figs. 4, 5, 7, 8). Results from ICP (Fig. 7A, 7B) show the
 535 estimated vertical motion for an area of 2.25 km². In this case, subsidence increases from
 536 southwest to northeast. ICP using LiDAR ground points (Fig. 7A) indicates that the uplift region
 537 on the southern block is small while the northern block experienced greater subsidence.

538 With ICP with LiDAR points on stable surfaces, we detected that the uplift area is larger:
 539 mostly across the southern block. Again, we estimate more subsidence in the northern block than
 540 in the southern block (Fig. 7B). The errors for this experiment are larger compared to the ones
 541 found using LiDAR ground points, although this was expected due to the lack of stable surfaces
 542 in 1999 in comparison to the ones found in 2018.

543 In comparison to the SJB1 GNSS station, which shows a vertical motion between 1999-
 544 2018 of -25.65 mm, the results using LiDAR ground points are almost four times larger than the

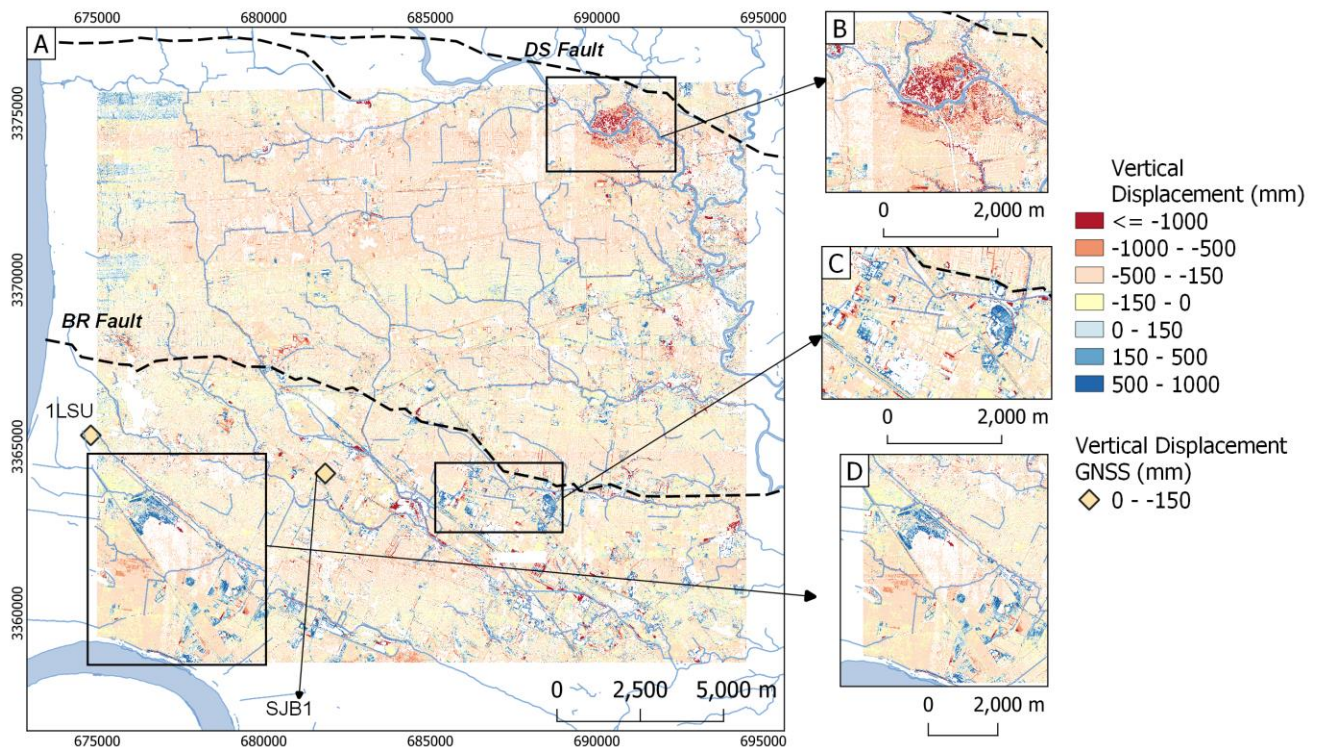
545 estimates from the station, and the results from the points of the stable surface are almost two
 546 times larger. It is worth to remember that since the GNSS station is anchored at some unknown
 547 depth, each tool may be measuring different processes.



548
 549 **Figure 7:** Vertical displacement calculated from ICP algorithm. (A) Mean displacement using LiDAR ground
 550 points. (B) Mean displacement using stable surfaces LiDAR points. (C) Margin of error of the results for (A). (D)
 551 Margin of error of the results for (B). Each circle in A and B represents the mean displacement of an area of 2.25
 552 km². Errors in C and D are calculated as the margin of error with respect to the mean. Rhombus are the vertical
 553 displacement calculated using rate from the GNSS CORS stations for 19 years. Base map imagery from
 554 QuickMapServices - QGIS (Map data ©2015 Google). Systematic errors are calculated as the average difference
 555 between the fourth row from north to south of (A) and (B).

556 We calculated Vertical DEM differencing 1) without co-registration; 2) with co-
 557 registration using ground points; and 3) with co-registration using points on stable surfaces.
 558 Results without co-registration show mean displacements per block larger than 300 mm in the 19
 559 years of analysis and more extreme values at individual locations; these values are not coherent
 560 with other estimates nor the features in the area. We, therefore, only keep the results from co-
 561 registered DEMs. We are just presenting the results for co-registration with ground points (Fig.
 562 8) because these results and the ones co-registered with stable surface points present similar

563 patterns, but the sample of points here is larger for co-registration. The mean vertical
 564 displacement for the northern block is -211.86 mm and for the southern block it is -133.09 mm.
 565 Errors are found in Table 2. For this analysis the errors (MOE) are small due to the large number
 566 of pixels on each block. These results show again more subsidence in the northern block than in
 567 the southern block. Empty pixels in Figure 8 do not have results because there are water bodies,
 568 high vegetation density, or the values were below the propagated error for each subarea of 2.25
 569 km². Insets show areas of interest for the discussion section.



570 **Figure 8:** Vertical displacements calculated from Vertical DEM differencing. (A) Vertical displacements calculated
 571 the co-registered DEM using results from ground points. (B, C, D) Some areas of interest discussed in the text.
 572

573 All our estimates and main statistics are summarized in Table 2. These values are
 574 averaged estimates for the whole block calculated using the results in that area, rather than
 575 individual locations. This table does not include the residual systematic errors that may affect the
 576 data for InSAR and LiDAR (Section 3.5). The former errors may be considered when looking at
 577 individual locations.

578 **Table 2:** Main statistics per block for each tool. MOE stands for Margin of Error. Numbers marked with a * refer to
 579 values derived from the estimates. These numbers do not have an estimated error and are for comparison purposes.
 580 All the values are in NAD83. The InSAR displacements correspond just to the period indicated in the column Time
 581 Span. The LOS rates for the GNSS stations are the projections of the rates using the parameters for each satellite.

582

PSI (LOS direction)						
Dataset	Time Span	Block	Mean velocity (mm/y)	Median velocity (mm/y)	MOE of the mean velocity (mm/y)	Mean displacement (mm)
EnviSAT	2004-2010	Northern	-10.869	-11.225	0.0384	-65.214*
		Southern	-8.030	-7.839	0.0614	-48.181*
Sentinel-1	2017-2020	Northern	-13.65	-13.645	0.00471	-40.96*
		Southern	-10.559	-10.82	0.00895	-31.68*
ICP						
Dataset	Direction	Block	Mean velocity (mm/y)	Mean displacement (mm)	Median displacement (mm)	MOE of the mean displacement (mm)
Ground point cloud	Up	Northern	-8.385*	-159.313	-140.9	13.8
	North		2.51*	47.66	49.54	9.26
	East		13.964*	265.31	269.41	10.32
	Up	Southern	-5.124*	-97.352	-101.4	8.03
	North		1.162*	22.072	27.04	8.45
	East		13.845*	263.05	259.41	10.72
Stable point cloud	Up	Northern	-5.023*	-95.433	-117.89	19.671
	North		2.52*	47.866	25.04	13.155
	East		14.44*	274.389	295.9	15.638
	Up	Southern	-2.391*	-45.422	-82.89	28.75
	North		2.845*	54.056	56.04	12.192
	East		11.89*	225.9	225.9	19.595
DEM differencing						
Dataset	Direction	Block	Mean velocity (mm/y)	Mean displacement (mm)	Median displacement (mm/y)	MOE of the mean displacement (mm/y)
DEM's from Ground point clouds	Up	Northern	-11.15*	-211.859	-207.565	0.00014
	Up	Southern	-7.005*	-133.09	-167.9	0.00025
GNSS						
Station	Direction	Block	Mean velocity (mm/y)		Mean displacement (mm)	
1LSU	Up	Southern	-4.31		-81.89* (1999-2018)	
	North		2.66		50.54* (1999-2018)	
	East		13.39		254.41* (1999-2018)	

	LOS EnviSAT		-9.81	-58.86* (2004-2010)
	LOS Sentinel		-10.89	-32.6* (2017-2020)
SJB1	Up	Southern	-1.35	-25.65* (1999-2018)
	North		2.22	42.18* (1999-2018)
	East		13.69	260.11* (1999-2018)
	LOS EnviSAT		-7.23	-43.38* (2004-2010)
	LOS Sentinel		-8.4	-25.2* (2017-2020)

583

584 **5 Discussion**585 **5.1 InSAR time series and LiDAR differencing measurements**

586 We created time series with the PSI method using EnviSAT data between 2004 and 2010 and
587 Sentinel-1 data acquired between 2017 and 2020. The rates and displacements calculated with
588 this method are presented in the LOS direction. We are aware that there are significant horizontal
589 displacements in the study area because the two GNSS stations and LiDAR-ICP results show
590 displacements towards the north and east directions (Fig. 6). Owing to the horizontal
591 displacements, we cannot isolate vertical displacements from InSAR because we only have one
592 geometry for the SAR acquisitions, but we can compare the observations in the LOS direction to
593 the vertical results from LiDAR (Zhong et al., 2022). PSI uses persistent scatterers on the surface
594 to estimate their deformation, making this methodology appropriate for urban areas such as
595 Baton Rouge (e.g., Ferretti et al., 2004). One must be cautious, however, with the interpretation
596 of these results because they incorporate the signal of all the processes affecting the base of the
597 persistent scatterer (e.g., Crosetto et al., 2016). One of the processes that may shape the results
598 from the InSAR time series is the seasonal variations from the hydrological cycle (Li et al.,
599 2020); for both datasets, most of the images were acquired during dry periods between October
600 to April (Table S1). Then, if there is any elastic deformation caused by seasonal changes in water
601 mass, it would appear more positive than negative due to the acquire dates of our images.
602 Seasonal loading may increase the rates (Figs. 4, 5). If the rates are influenced by seasonal
603 rebound, then subsidence may be larger than the rates reported with InSAR time series, based on
604 comparison to hydrological models (e.g., Puskas et al., 2017; Chen et al., 2023).

605 The two LiDAR surveys used here were acquired over similar seasonal conditions. Then,
606 ICP and LiDAR differencing probably are measuring net changes between the surveys with little
607 impact of the seasonal cycles, although uncertainties must be considered for individual locations.
608 The results are more affected by the LiDAR point cloud with the worst resolution: the 1999
609 survey.

610 One of the advantages of using LiDAR data is that it allows one to separate the information
611 into surfaces of interest such as ground points and stable surfaces. We used this approach (Fig. 6
612 and 7) to estimate the displacement in the three components of surfaces that are at different
613 elevations or anchored in the subsurface. Just as InSAR, these methods measure signals of all the
614 processes that affect the base of the point. Here we take advantage of the spatial resolution of
615 LiDAR and averaged pixels to improve the results that can be affected by the low vertical
616 accuracy of the 1999 survey. With LiDAR we estimate the vertical and horizontal components of
617 displacement between the two surveys using ICP, which goes a step further than just the
618 estimates of vertical motion taken by Zhong et al. (2022). ICP estimates indicate that most of the
619 horizontal motion is towards the east in both blocks (Fig. 6), agreeing with the GNSS stations in
620 the area. Nevertheless, the horizontal displacements estimated with stable ground points (Fig.
621 6B) have more variations and seem to indicate more motion towards the north in comparison to
622 the ones estimated with ground LiDAR points, particularly near the eastern segment of the BRF
623 (Fig. 6). It is worth noting that the difference between the results from ground and stable LiDAR
624 points may indicate anomalies near the fault segment at different depths, but also may be caused
625 by the lack of stable surfaces in some areas in 1999 before rapid urban growth between 2005-
626 2010 (Supplemental Material – gif 1). The sharp change between the results using LiDAR
627 ground and stable points in the northern block (Fig. 7) may be caused by residual systematic
628 errors left after co-registration of the surveys (Section 3.6). This area marks the edge between
629 files from the 2018 point cloud. Systematic errors similar to the ones observed here have been
630 reported in previous research with topographic LiDAR data (e.g., Anderson, 2019).

631 **5.2 Comparison of LiDAR differencing, InSAR time series and GNSS records**

632 LiDAR results, ICP and differencing all indicate that the northern block is subsiding
633 faster than the southern block with respect to the 1LSU GNSS station. The InSAR time series
634 also indicates that the northern block is moving away from the satellite faster than the southern
635 block. It is, therefore, reasonable to assume that the vertical motion is dominating the

636 measurements, and it is very likely that the north component is negligible (e.g., Samieie-
637 Esfahany et al., 2010). From InSAR measurements, it is possible to see that the BRF serves as a
638 boundary between the areas of rapid and slow subsidence (Fig. 4 and 5). This behavior, however,
639 contradicts the long-term displacement of the down-to-south normal fault from seismic imaging
640 (e.g., Fig. 1).

641 The mean vertical rates from ICP vary between -8.4 to -5 mm/y in the northern block and
642 -5.1 to -2.4 mm/y in the southern block. Sentinel-1 rates in the LOS direction are larger than the
643 ICP vertical rates by ~5 mm/y in both blocks. We can, therefore, infer that the results are not just
644 comparable in magnitude but consistent, and that the northern block is subsiding faster than the
645 southern block.

646 In the southern block, there are two GNSS stations. We used the 1LSU station to tie the
647 results and SJB1 for comparison. These stations show that the southern block is subsiding and
648 moving horizontally E-NE in the NAD83 reference frame. This motion agrees with the direction
649 of the ICP results. The E-NE horizontal motion from the GNSS stations and ICP is likely due to
650 the definition of the NAD83 reference frame with plate fixed as indicated by horizontal velocity
651 models for North America (e.g., Snay et al., 2013; Robin et al., 2020). These results also suggest
652 shallow vertical slip rather than rotational slip along the BRF.

653 The velocity from Sentinel-1 InSAR time series on the building hosting SJB1 ranges
654 between -9 to -12 mm/y in the LOS direction, while SJB1 has a velocity of -8.40 mm/y (Fig. 4).
655 This difference can be caused by the length of the time series of each case; SJB1 rate is
656 calculated with data since 2010 while InSAR only covers 2017-2020. Changes in the station may
657 also play a role, but still, there is agreement among all the three tools. The two nearby GNSS
658 stations have different vertical motion rates (Section 2.4, Table 2; Fig. S3). The difference in
659 amplitude may appear as uncertainty in the InSAR data after tying to GNSS, whereas it is most
660 likely a local geological effect caused by the local response to groundwater changes. SJB1's
661 magnitude is better replicated by the results with stable LiDAR points (Fig. 7 and Table 2).

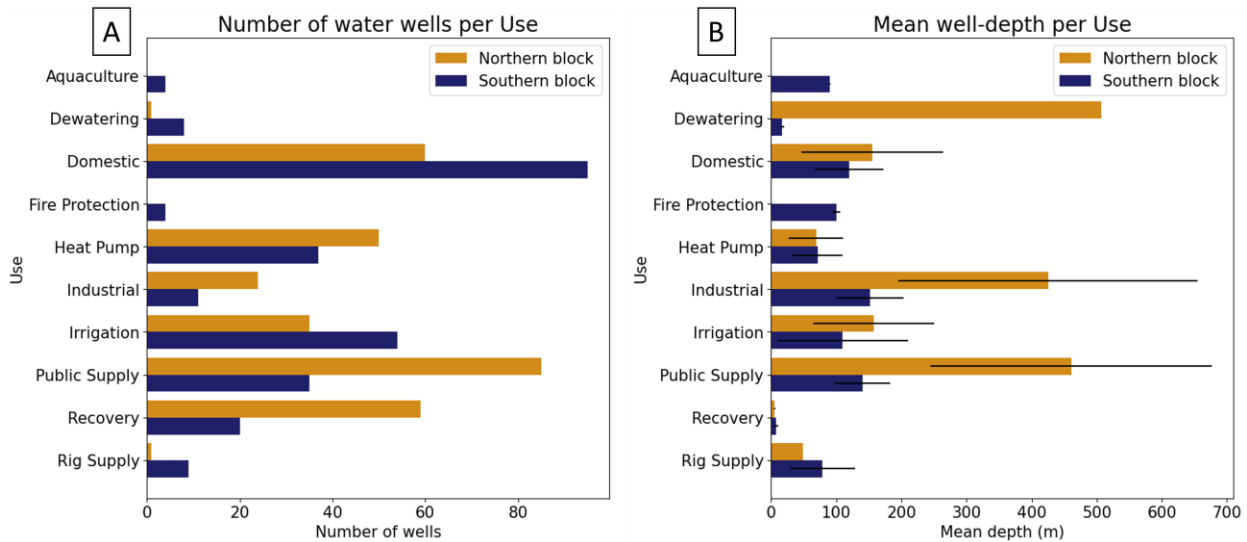
662 **5.3 Relation with anthropogenic activities**

663 Results from LiDAR differencing provide good estimates to detect trends of changes in
664 small areas due to their high spatial resolution. These results show the spatial trends of the
665 complete study area and the changes caused by human construction. For instance, the

666 construction of the FedEx facility in 2014, the Ochsner Medical Complex in 2017, the Woman's
667 hospital in 2010, and some new home complexes between 2006-2017 are seen in Figures 8C and
668 8D. Although these changes are visible with LiDAR, we consider that urban growth and new
669 constructions are not the main factors decelerating the rates in the southern block, or accelerating
670 them in the northern block, because urban growth has occurred across Baton Rouge
671 (Supplemental Material – gif, Fig. S6). There are multiple examples of construction with similar
672 characteristics in the northern block that do not affect the general spatial trend of the fault block
673 (Fig. S6). The 2000, 2010, and 2020 censuses indicate that the city's population has increased by
674 almost 10% (~44,000 new inhabitants) with most of this increase occurring during the first decade
675 and soon after Katrina (U.S. Census Bureau, 2003; 2012; 2021). The areas in the southern block
676 with smaller rates are recorded in LiDAR ICP, vertical DEM differencing, and in both InSAR
677 time series.

678 During the study period 2034 water wells were active, with 592 of them extracting water
679 for multiple purposes (Fig 9, Table 1). The remaining wells monitored groundwater quality and
680 level mostly near industrial wells, close to areas of injection or oil and extraction, and near the
681 western and middle segments of the BRF. Most of the groundwater in East Baton Rouge is used
682 for industrial and public supply. These uses are recognized to cause most of the decline of the
683 groundwater levels in the region and saline intrusions near the BRF (Tomaszewski et al., 2002;
684 Anderson et al., 2013). Groundwater studies indicate the aquifers in the northern block recharge
685 from infiltration in areas north of the DSF (Tomaszewski et al., 2002; Vahdat-Aboueshagh and
686 Tsai 2021), while the aquifers in the southern block are filled mostly with saline water from the
687 GOM (Fig. 1). It is known that groundwater withdrawal in the Baton Rouge district surpasses
688 recharge, causing the decline in groundwater levels (White, 2017). There are more water wells in
689 the northern block than in the southern block for almost all uses due to the salinity charge (Fig.
690 9A). Also, most wells are at deeper depths in the northern block (Fig. 9B). The mean depth for
691 industrial and public supply wells is between 400-500 m, probably reaching the deeper sand
692 layers (1500 and 2000-ft sands). These aquifers have been greatly affected by pumping water
693 (Tomaszewski et al., 2002; Nasreen, 2003; Elshall et al., 2013), and have developed cones of
694 depression (Chen et al., 2023). On the other hand, the southern block has fewer water wells
695 extracting water, which is more saline, and are at shallower depths. Our results support the
696 hypothesis that the northern block is part of a regional depression cone caused by water

697 extraction and observed in previous groundwater models (e.g., Chen et al., 2023). This may
 698 explain the general trend of subsidence displacements increasing from south to north with
 699 LiDAR and in the LOS direction with InSAR time series.



700 **Figure 9:** Water well statistics per block in the study area. (A) Number of wells per use. (B) Mean depth of water
 701 wells per use. Lines indicate standard deviation of the well depth values. Well data from the Louisiana Department
 702 of Natural Resources (SONRIS), (n.d.).
 703

704
 705 The relationship between groundwater withdrawal and subsidence is known and supported
 706 by several studies globally (e.g., Guzy and Malinowska, 2020; Fiaschi and Wdowinski, 2020).
 707 Jones et al., (2016) concluded that groundwater withdrawal caused subsidence in the Michoud
 708 area in New Orleans. They found that areas around chemical plants or refinery facilities with
 709 water wells have larger subsidence rates than areas without these wells. The area with largest
 710 subsidence in our study area was detected with LiDAR methods (Fig. 7 and 8B), while in InSAR
 711 time series it is masked by dense vegetation. This region does not have water wells, but there are
 712 15 water wells that were active during the study period within a radius of 2 km, seven of which
 713 are of domestic use at the north and east, five for public supply in the west and south, three for
 714 irrigation in the west direction (Fig. S7). Another factor that should not be ignored is the
 715 proximity to the Comite river at the eastern edge of the study area (Fig. 3) and its interaction
 716 with the aquifers in this area. Chen et al. (2023) argue that the Comite river does not have
 717 important interactions with the Southern Hills aquifer system, although locally this area remains
 718 an open question.

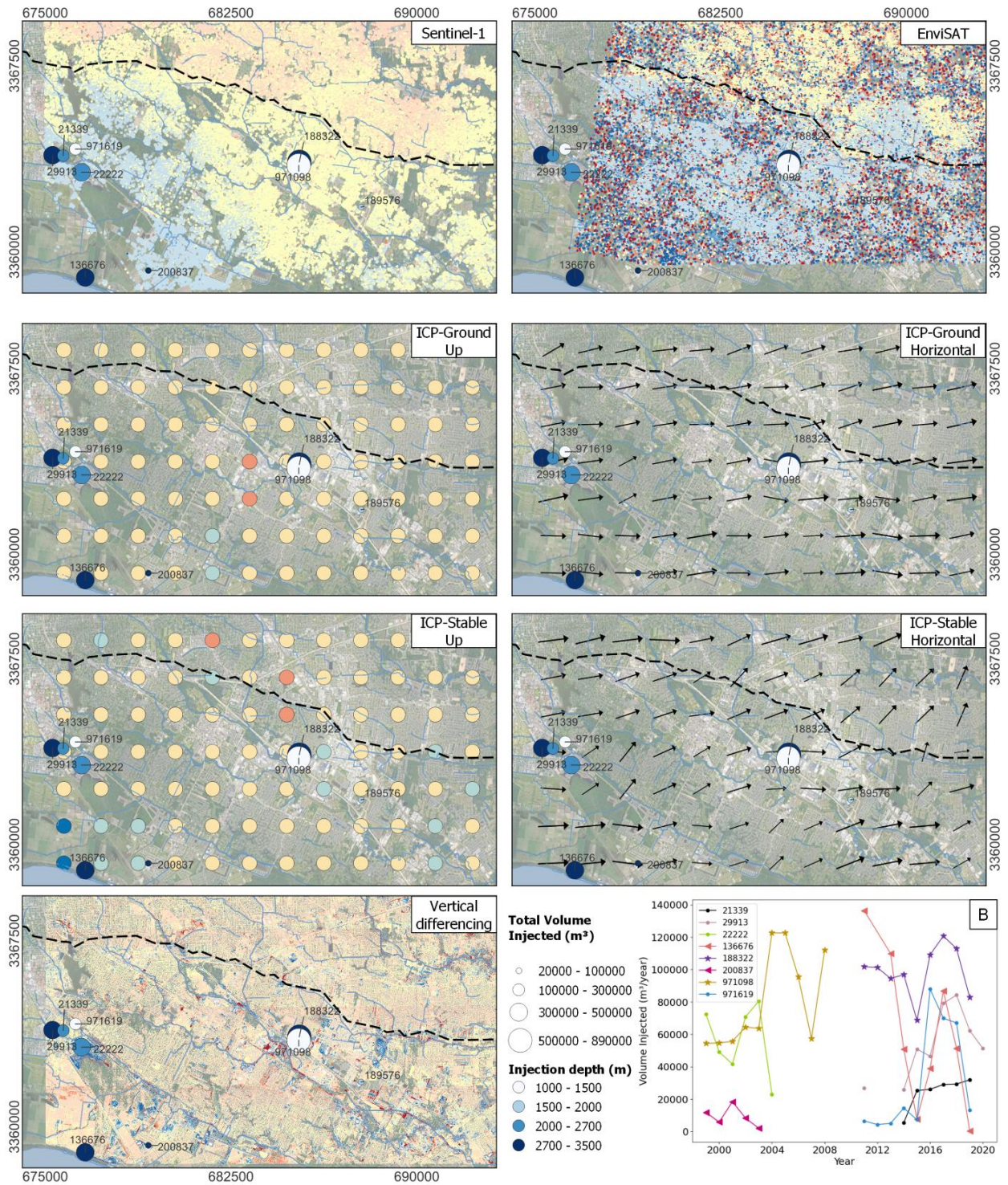
719

720 Figures 8C and 8D show the areas with the smallest subsidence displacements in the study
721 area. These areas have most of the injection and oil/gas extraction wells (Fig. 2, S4, Table 1).
722 Ten of these wells injected saline waters at depths between 1445-3155 m. The other injection
723 wells are at ~15 m depth and are not included in these areas. Multiple studies have shown that
724 injection of fluids can increase pore pressure at depth which can diffuse and cause local uplift
725 (e.g., Teatini et al., 2011; Anderson et al., 2013; Shirzaei et al., 2016). Shirzaei et al., (2016)
726 related injection of fluids with large surface displacement and earthquakes in Texas. For their
727 model they calculated a volume change of 700.000 m³/y which is close to the injection volume
728 of their area. Consequently, an increase in subsurface pressure caused by injection can be an
729 explanation for the slower displacements and rates in the southern block (e.g., Fig, 4C point P6).
730 We compare the depth and injected volume of the injection wells with our results (Fig. 10) to see
731 if there is any evidence of change of the surface that could be related to them. Our study area
732 does not have a total injection above 300,000 m³/y during the study period (Fig. 10), suggesting
733 that pressures are not yet large enough to induce earthquakes.

734 One interesting example of the possible signals of injection are the wells identified as 971098
735 and 188322 (Fig. 10). They are separated by ~ 200 m and both injected a similar volume of
736 saline water. The first one injected water before 2008, while the second experienced fluid
737 injection between 2011 and 2019. Besides the period of injection, these two wells differ in the
738 depth of injection: Well 971098 bottoms at ~1500 m whereas 188322 bottoms at ~3000 m. The
739 two injection depths fill different sand bodies, but the shallower well is expected to contribute
740 more to the observed relative uplift of the southern block; there is not a strong signal from the
741 deeper well in the Sentinel-1 dataset. This was expected due to the disposal depth of the wells.
742 Another example is the four wells in the western part of the study area (Fig. 10). The distance
743 among these is less than 1 km. The depth of these wells varies between ~1500 to ~3000 m. The
744 complete area seems to be moving at slower rates than the northern block, but it is not possible to
745 disentangle the signal caused by each injection well. Our observations indicate that the BRF may
746 be acting as a barrier preventing flow of the injected fluids to the northern block (e.g., Shirzaei et
747 al., 2016).

748 We perform a similar comparison with the oil and gas wells (Figs. S4, S8). All of these wells
749 have bottom hole depths deeper than 1700 m, and most are near the injection wells which are at
750 shallower depths. It is not possible to say whether these wells are causing any change in our

751 results, and therefore we cannot conclude that oil and gas extraction during the study period
 752 caused any change on the surface.



753

754

755

Figure 10: Injection volumes and depth shown in all our results. **B)** Time series of volumes injected by each well in the study area between 1999 and 2020.

756 **5.4 Geological factors**

757 The study area has multiple factors that may contribute to vertical crustal movement that are
758 difficult to deconvolve, but sediment compaction is minimal. Our results from InSAR time series
759 and LiDAR show that the entire area is subsiding, but that the BRF marks the boundary between
760 faster and slower subsiding areas (Figs 4-8). These results agree with groundwater models of the
761 region. The sharp change in vertical crustal movement along some sectors of the BRF suggests
762 that BRF remains a hydrological divide, but we cannot determine whether parts or all the fault
763 slipped episodically or continuously between 1999 and 2020. The rates that we determined
764 (Table 2) are two orders of magnitude larger than the time-averaged fault slip rate from Shen et
765 al. (2017) (~ -0.02 mm/y) and are comparable or larger than the ~ 3 mm/y from Hopkins et al.,
766 (2021) for some segments of BRF. The correlation of changes in vertical crustal motions with
767 injection and water wells indicates that anthropogenic activities have increased BRF slip rates,
768 but we cannot conclude much about the DSF due to the lack of information in the area.

769 We present four examples of individual structures' motion along the BRF (Fig. S9;
770 Supplemental material - T2). It is important to highlight the examples in the center area of the
771 fault that show more motion than those near the eastern and western limits, although the
772 foundations of examples are unknown and, in some cases, the number of PSIs is very small. We
773 recommend further investigation of individual structures with InSAR time series and/or ground
774 leveling campaigns.

775 Horizontal displacement from ICP in the eastern portion of the BRF shows an apparent
776 change of direction (Fig 6). Despite the large uncertainties, this can be an area of future research
777 because 1) the Nesser and Siegen oil fields are nearby in the southern block and were exploited
778 during the study period, 2) in August of 2016, the Amite River (Fig. 3) flooded affecting the
779 eastern part of the study area which may influence the time-averaged estimates in the area.

780 **5.5 Future Implications**

781 Vertical crustal motion occurred in the Baton Rouge sector of the GOM passive margin since
782 1999, as detected here with InSAR and LiDAR methods, and corroborated by sparse GNSS data.
783 These vertical crustal movements may be an indicator of groundwater storage changes and
784 recharge characteristics for the aquifers under the study area. These motions may also indicate
785 how injection at shallow depths is deforming the surface. The BRF zone serves as a boundary

786 between two differentially subsiding blocks, indicating that it may also separate distinct
787 hydrographic domains, and that it localizes differential motion. Hydrological studies indicate
788 that the aquifers in the northern block are more affected by groundwater withdrawal than those in
789 the south (e.g., Elshall et al., 2013). The subsidence rates in the northern block increase from the
790 BRF towards the DSF, and in the southern block subsidence increases south of the BRF, where
791 saline water infiltrates sand bodies and where saline wastewater is injected (Nasreen, 2003;
792 Elshall et al., 2013; White, 2017). Our results agree with recent groundwater change models of
793 Chen et al. (2023). They show that the average groundwater levels between 2004 and 2020 were
794 low (-10 to -20 m) in Baton Rouge between the BRF and the DSF. This area is part of the local
795 cone of depression caused by the large water extraction of deep aquifers at 400-900 m depth. Our
796 results in the northern block may be the surface expression of the changes in groundwater
797 storage (i.e., the cone of depression) caused by the decline of groundwater levels showed on
798 Chen et al., (2023).

799 East Baton Rouge is one of the most populated parishes in Louisiana and likely its population
800 will grow as it has done it in the last 20 years (U.S. Census Bureau, 2003; 2012; 2021). Besides,
801 due to climate changes expected for the ongoing century in the GOM (Pendleton et al., 2010;
802 Frederikse et al., 2020; Dangendorf et al., 2023), coastal retreat from regions vulnerable to storm
803 surge and wind damage from hurricanes will continue to drive population growth (e.g., Qiang
804 and Lam, 2016) as has happened before (Sastry, 2009). Simultaneously, as the population grows,
805 water consumption likely will increase. Considering vertical surface changes as a proxy for
806 groundwater level and storage changes, it is important to protect the aquifers underlying the area
807 from saline water intrusions and groundwater level decline. These actions will also protect the
808 surface from non-natural changes.

809 There are many wells whose purpose is to monitor local groundwater, but just two GNSS
810 stations to study surface elevation changes; they are wholly inadequate to track BRF movement.
811 The localized fault slip along the BRF and differential ground subsidence motivates continuous
812 monitoring at local and regional scales to track surface elevation changes associated with fluid
813 extraction and injection.

814 **6 Conclusions**

815 This study presents a detailed regional panorama of the relationship between injection and
816 extraction of fluids and vertical and horizontal surface displacements. We also show how
817 geodetic methods can be used to estimate vertical and horizontal displacements in areas with
818 slow motions for the first-time using LiDAR data with the ICP algorithm. InSAR time series
819 with PSI is a suitable method for urban areas such as Baton Rouge and shows similar results to
820 LiDAR in the LOS direction after GNSS corrections. We verify our results using ground
821 measurements from permanent GNSS stations. The agreement of the results from the three
822 datasets on the same reference system offers insight into the reliability of LiDAR to estimate
823 vertical and horizontal motion. We reiterate the need for more GNSS stations in the area,
824 particularly in the northern block, to adequately track the motion of the BRF and to better
825 constrain the results from other geodetic methods.

826 We selected East Baton Rouge as the study area because the deformation signal caused by
827 fault slip and anthropogenic activities should control vertical ground motion. Our results show
828 that the entire area is subsiding, but subsidence reverses the long-term, down-to-the-south
829 displacement. We observe that the BRF divides the study area into two different regions of
830 mostly human-controlled subsidence: 1) Subsidence in the northern block is likely controlled by
831 groundwater level changes caused by pumping and it is sinking faster than the southern block
832 showing a cone of depression. These results are supported by recent groundwater models. 2)
833 Subsidence in the southern block, which is influenced by the injection of fluids at shallow depths
834 that may be causing volumetric expansion and less water pumping. It is important to remember
835 that seasonal contributions can influence the results from InSAR time series, and it is something
836 to consider in future analysis. Horizontal motions estimate from ICP show that the area is
837 moving to the east with a small displacement to the north. This agrees with the estimates from
838 GNSS.

839 Considering the future climate change scenarios where population displacement and water
840 scarcity are likely, it is important to consider these observations for future city planning to ensure
841 the conservation and protection of the aquifers in the area, and to minimize the effects of saline
842 infiltrations through the BRF.

843

844 **Acknowledgments**

845 CH and CE were supported by funds from the Marshall-Heape endowment to Tulane
846 University and from training opportunities offered by UNAVCO (Earth Scope). CH and CE
847 grateful acknowledge support from the Marshall-Heape endowment to Tulane University. CH
848 thanks the conversations with JL. Whitten and K. Materna about the development of this work
849 and S. Villamarin about the statistical background. This manuscript benefited from conversations
850 with R. Arrowsmith. Thanks to reviewers Artur Guzy and the other anonymous reviewers for the
851 feedback that helped to improve this research.

852 **Open Research**

853 **Data Availability Statement**

854 LiDAR data from 1999 is stored and distributed by the Atlas: The Louisiana Statewide GIS
855 (<https://maps.ga.lsu.edu/lidar2000/>). LiDAR data from 2018 is stored and distributed by the
856 USGS Server through The National Map Download Manager
857 (<https://apps.nationalmap.gov/downloader/>).

858 EnviSAT SAR images were retrieved from the Earth Observation Catalogue
859 (<https://eocat.esa.int/sec/#data-services-area>). Sentinel-1 SAR images from the Copernicus Open
860 Access Hub (<https://scihub.copernicus.eu/dhus/#/home>). Both property of the European Space
861 Agency.

862 GNSS information was processed by the Nevada Geodetic Laboratory (Blewitt et al., 2018;
863 <http://geodesy.unr.edu/NGLStationPages/gpsnetmap/GPSNetMap.html>).

864 Data from water, injection, and extraction wells is stored in the Strategic Online Natural
865 Resources Information System property of the Louisiana Department of Natural Resources
866 (<http://sonris-www.dnr.state.la.us/gis/agsweb/IE/JSViewer/index.html?TemplateID=181>).

867 LiDAR and InSAR results are available in a data repository (Hurtado-Pulido et al., 2023).

868

869 **Software Availability Statement**

870 LiDAR data was filtered to create stable surface clouds and DEMs were created using the Point
871 Data Abstraction Library (PDAL, 2018). The ICP algorithm was run using the MATLAB code
872 created by Scott et al. (2020) that uses the LIBICP software (Geiger et al, 2012). The
873 Geomorphic Change Detection software (GCD) was used to create the DEMs of Differences
874 (Wheaton et al., 2010). InSAR time series were processed using SARscape (2021) software.

875 Spatial analysis and maps were done with QGIS v. 3.18 (2018). Figures were done using
876 Matplotlib on Python (Hunter, 2007).

877 **References**

- 878 Andersons, S., (2019). Uncertainty in quantitative analyses of topographic change: error
879 propagation and the role of thresholding. *Earth surface processes and landforms*. 44 (5),
880 1015-1033. doi: 10.1002/esp.4551
- 881 Anderson, C., Hanor, J., Tsai, F., (2013). Sources of salinization of the Baton Rouge aquifer
882 system, Southeastern Louisiana. *Gulf Coast Association of Geological Societies*
883 *Transactions*. 63, 3-12.
- 884 Blewitt, G., Hammond, W., Kreemer, C., (2018), Harnessing the GPS data explosion for
885 interdisciplinary science. *Eos*, 99, <https://doi.org/10.1029/2018EO104623>
- 886 Blum, M., & Roberts, H. (2012). The Mississippi delta region: Past, present, and future. *Annual*
887 *Review of Earth and Planetary Sciences*, 40, 655-683. doi:10.1146/annurev-earth-042711-
888 105248
- 889 Brook, A., and Ben-Dor, E., (2011). Automatic registration of airborne and spaceborne images
890 by topology map matching with SURF processor algorithm. *Remote Sensing*, 3 (1), 65-82.
891 doi:10.3390/rs3010065
- 892 Chan, Y., Koo, V., (2008). An introduction to Synthetic Aperture Radar (SAR). *Progress in*
893 *Electromagnetics Research*, 2, 27-60. doi:10.2528/PIERB07110101
- 894 Chan, A., and Zoback, A., (2007). The role of hydrocarbon production on land subsidence and
895 fault reactivation in the Louisiana Coastal Zone. *Journal of Coastal Research*, 23 (3), 771-
896 786. doi: 10.2112/05-0553
- 897 Chen, Y., Vahdat-Aboueshagh, H., Tsai, F., Dausman, A., Runge, M., (2023). Unstructured-grid
898 approach to develop high-fidelity groundwater model to understand groundwater flow and
899 storage responses to excessive groundwater withdrawals in the Southern Hills aquifer
900 system in southeastern Louisiana (USA). *Journal of Hydrology: Regional Studies*. 46. doi:
901 10.1016/j.ejrh.2023.101342
- 902 Church, J., Clark, P., Cazenave, A., Gregory, J., Jevrejeva, S., Levermann, A., Merrifield, M.,
903 Milne, G., Nerem, R., Nunn, P., Payne, A., Pfeffer, W., Stammer D., and Unnikrishnan, A.,
904 (2013). Sea Level Change. In: *Climate Change 2013: The Physical Science Basis*.
905 Contribution of Working Group I to the Fifth Assessment Report of the Intergovernmental
906 Panel on Climate Change [Stocker, T., Qin, D., Plattner, G., Tignor, M., Allen, S.,
907 Boschung, J., Nauels, A., Xia, Y., Bex V., Midgley, P., (eds.)]. Cambridge University Press,
908 Cambridge, United Kingdom and New York, NY, USA.
- 909 Crossetto, M., Moserrat, O., Cuevas-Gonzalez, M., Devanthery, N., Crippa, B., (2016). Persistent
910 Scatterer Interferometry: A review. *ISPRS Journal of Photogrammetry and Remote Sensing*.
911 115, 78-89. doi:10.1016/j.isprsjprs.2015.10.011
- 912 Culpepper, D., McDade, E., Dawers, N., Kulp, M., and Zhang, R., (2019a). Synthesis of fault
913 traces in SE Louisiana relative to infrastructure (Project No. 17GTL SU12). *Transportation*
914 *Consortium of South-Central States*. https://digitalcommons.lsu.edu/tranсет_pubs/30/

- 915 Culpepper, D., McDade, E., Dawers, N., Kulp, M., and Zhang, R. (2019b). Data from: synthesis
916 of fault traces in SE Louisiana relative to infrastructure. Retrieved from
917 https://digitalcommons.lsu.edu/transet_data/30
- 918 Dangendorf, S., Hendricks, N., Sun, Q., Klinck, J., Ezer, T., Frederikse, T., Calafat, F., Wahl, T.,
919 Tornqvist, T., (2023). Acceleration of U.S. Southeast and Gulf coast sea-level amplified by
920 internal climate variability. *Nature Communications*. 14 (1), 1-11. doi: 10.1038/s41467-023-
921 37649-9
- 922 Dokka, R., (2006). Modern-day tectonic subsidence in Coastal Louisiana. *Geology*. 34 (4), 225-
923 228. doi: 10.1130/G22264.1
- 924 Dokka, R. Sella, G., and Dixon, T. (2006). Tectonic control of subsidence and southward
925 displacement of southeast Louisiana with respect to stable North America: *Geophysical*
926 *Research Letters*, 33 (L23308). doi:10.1029/2006GL027250
- 927 Dokka, R. (2011). The role of deep processes in late 20th century subsidence of New Orleans
928 and coastal areas of southern Louisiana and Mississippi. *Journal of Geophysical Research*.
929 116 (B06403). doi:10.1029/2010JB008008.
- 930 Durham, C., and Peoples E., (1956). Pleistocene fault zone in southeastern Louisiana. *Gulf Coast*
931 *Association of Geological Societies Transactions*. 6, 65-66.
- 932 Eddy, D., Van Avendonk, H., Christeson, G., Norton, I., Karner, G., Johnson, C., Snedden, J.,
933 (2014). Deep crustal structure of the northeastern Gulf of Mexico: Implications for rift
934 evolution and seafloor spreading. *Journal of Geophysical Research: Solid Earth*. 119 (9),
935 6802-6822. doi: 10.1002/2014JB011311
- 936 Elshall, A., Tsai, F., Hanor, J., (2013). Indicator geostatistics for reconstructing Baton Rouge
937 aquifer-fault hydrostratigraphy, Louisiana, USA. *Hydrogeological Journal*. 21 (8), p. 1731-
938 1747. doi: 10.1007/s10040-013-1037-5
- 939 European Space Agency, (ESA) (2021a). Earth Observation Catalogue – EO CAT. EnviSAT
940 images. Last visited July/2022. Retrieved from <https://eocat.esa.int/sec/#data-services-area>
- 941 European Space Agency, (ESA) (2021b). Copernicus Open Access Hub. Sentinel-1 images. Last
942 visited July/2022. Retrieved from <https://scihub.copernicus.eu/dhus/#/home>
- 943 Fattahi, H., Amelung, F., (2014). InSAR uncertainty due to orbital errors. *Geophysical Journal*
944 *International*. 199 (1). 549-560. doi: 10.1093/gji/ggu276
- 945 Ferretti, A., Prati, C., Rocca, F., (2001) Permanent scatterers in SAR interferometry. *IEEE*
946 *Transactions on Geoscience and Remote Sensing*. 39 (1), 8–20. doi:10.1109/36.898661
- 947 Ferretti, A., Novali, F., Burgmann, G., Hiley, G., Prati, C., (2004). InSAR permanent scatterer
948 analysis reveals ups and downs in San Francisco Bay area. *Journal of Geophysical*
949 *Research: Solid Earth*. 85, 317-324. doi: 10.1029/2002jb002267
- 950 Ferretti, A., Savio, G., Barzaghi, R., Borghi, A., Musazzi, S., Novali, F., Prati, C., Rocca, F.,
951 (2007). Submillimeter accuracy of InSAR time series: Experimental validation. *IEEE*
952 *Transactions on Geoscience and Remote Sensing*. 45(5), 1142-1153. doi:
953 10.1109/TGRS.2007.894440
- 954 Fiaschi, S., and Wdowinski, S., (2020). Local land subsidence in Miami Beach (FL) and Norfolk
955 (VA) and its contribution to flooding hazard in coastal communities along the U.S. Atlantic
956 coast. *Ocean and Coastal Management*. 187. doi:10.1016/j.ocecoaman.2019.105078

- 957 Frederikse, T., Landerer, F., Caron, L., Adhikari, S., Parkes, D., Humphrey, V., Dangendorf, S.,
 958 Hogarth, P., Zanna, L., Cheng, L., and Wu, Y., (2020). The causes of sea-level rise since
 959 1900. *Nature*. 584 (7821), 393–397. doi:10.1038/s41586-020-2591-3
- 960 Gagliano, S., Meyer-Arendt, K., Wicker, K., (1981). Land loss in the Mississippi River deltaic
 961 plain. *Gulf Coast Association of Geological Societies Transactions*. 31, 295-300
- 962 Gagliano, S., Burton Kemp III, E., Wicker, K., and Wiltenmuth, K., (2003a). Active geological
 963 faults and land change in southeastern Louisiana (Contract No. DACW 29-00-C-0034). *U. S.*
 964 *Army Corps of Engineers*. <https://biotech.law.lsu.edu/katrina/govdocs/faults.pdf>
- 965 Gagliano, S., Burton Kemp III, E., Wicker, K., Wiltenmuth, K., and Sabate, R., (2003b). Neo-
 966 tectonic framework of southeast Louisiana and applications for coastal restoration.
 967 *Transactions of the 53rd The Gulf Coast Association of Geological Societies and the Gulf*
 968 *Coast Section SEMP*. 262-272
- 969 Gasparini, N., Fischer, G., Adams, J., Dawers, N., Janoff, A., (2015) Morphological signatures of
 970 normal faulting in low-gradient alluvial rivers in South-eastern Louisiana, USA. *Earth*
 971 *Surface Processes and Landforms*. 41, 642-657. doi: 10.1002/esp.3852
- 972 Geiger, A., Lenz, P., and Urtasun, R., (2012). Are we ready for autonomous driving the KITTI
 973 vision benchmark suite. 2012 IEEE Conference on Computer Vision and Pattern
 974 Recognition. 3354-3361. doi: 10.1109/CVPR.2012.6248074. [Computer software]
 975 <http://www.cvlibs.net/software/libicp/>
- 976 Goldstein, R., Zebker, H., Werner, C., (1988). Satellite radar interferometry: Two-dimensional
 977 phase unwrapping. *Radio Science*. 23 (4), 713-720. doi:10.1029/RS023i004p00713
- 978 Guzy, A., Malinowska, A., (2020). State of the art and recent advancements in the modelling of
 979 land subsidence induced by groundwater withdrawal. *Water*. 12 (7). doi:10.3390/w12072051
- 980 Hooper, A., Zebker, H., Segall, P., Kampes, B., (2004). A new method for measuring deformation
 981 on volcanoes and other natural terrains using InSAR persistent scatterers. *Geophysical*
 982 *Research Letters*. 31 (23), L23611. doi:10.1029/2004GL021737.
- 983 Hopkins, M., Lopez, J., Songy, A., (2021). Coastal Subsidence Due to Faults: Insights from
 984 Elevation Profiles of Vehicular Bridges, Southeastern Louisiana, U.S.A. *Journal of Coastal*
 985 *Research*. 38(1), 52-65. doi:10.2112/JCOASTRES-D-21-00015.1
- 986 Hunter, J., (2007). Matplotlib: A 2D Graphics Environment. *Computing in Science &*
 987 *Engineering*. 9 (3), 90-95. doi:10.5281/zenodo.592536
- 988 Hurtado-Pulido, C., Amer, R., Ebinger, C., Holcomb, H., (2023). Geodetic displacement data
 989 from Airborne-LiDAR data and Time Series InSAR: Baton Rouge Case Study [dataset]. doi:
 990 10.5281/zenodo.8187870
- 991 Jankowski, K., Törnqvist, T., Fernandes, A., (2017) Vulnerability of Louisiana’s coastal wetlands
 992 to present-day rates of relative sea-level rise. *Nature Communication*. 8 (14792).
 993 doi:10.1038/ncomms14792
- 994 Jones, C., An, K., Blom, R., Kent, J., Ivins, E., and Bekaert, D. (2016). Anthropogenic and
 995 geologic influences on subsidence in the vicinity of New Orleans, Louisiana. *Journal of*
 996 *Geophysical Research: Solid Earth*. 121 (5), 3867– 3887. doi:10.1002/2015JB012636
- 997 Karegar, M., Dixon, T., Malservisi, R., (2015). A three-dimensional surface velocity field for the
 998 Mississippi Delta: Implications for coastal restoration and flood potential. *Geology*. 43 (6),
 999 519-522. doi:10.1130/G36598.1

- 1000 Karegar, M., Dixon, T., Malservisi, R., Kushe, J., and Engelhart, S., (2017) Nuisance flooding
 1001 and relative Sea-Level Rise: the importance of present-day land motion. *Science Reports*. 7
 1002 (111997). doi:10.1038/s41598-017-11544-y
- 1003 Karegar, M., Larson, K., Kushe, J., and Dixon, T., (2020) Novel quantifications of shallow
 1004 sediment compaction by GPS Interferometric Reflectometry and implications for flood
 1005 susceptibility. *Geophysical Research Letters*. 47 (14). doi:10.1029/2020GL087807
- 1006 Keogh, M., and Törnqvist, T., (2019). Measuring rates of present-day relative sea-level rise in low
 1007 elevation coastal zones. *Ocean Science*, 15 (1), 61-73. doi:10.5194/os-15-61-2019
- 1008 Kuchar, J., Milne, G., Wolstencroft, M., Love, R., Taarasov, L., and Hijma, M., (2018). The
 1009 influence of sediment isostatic adjustment on sea level change and land motion along the
 1010 U.S. Gulf Coast: *Journal of Geophysical Research*, 123 (1), 780-796.
 1011 doi:10.1002/2017JB014695
- 1012 Kuecher, G., Roberts, H., and Thompson, M., (2001). Evidence for active growth faulting in the
 1013 Terrebone delta plain, South Louisiana: Implications for wetland loss and the vertical
 1014 migration of Petroleum. *Environmental Geosciences*, 8 (2), 77-94. doi:10.1046/j.1526-
 1015 0984.2001.82001.x
- 1016 Kulp, S., and Strauss, B., (2019). New elevation data triple estimates of global vulnerability to
 1017 sea-level rise and coastal flooding. *Nature Communications*. 10 (4844). doi:10.1038/s41467-
 1018 019-12808-z
- 1019 L3Harris. (2014, November). PS Tutorial – version 0.9. Retrieved April 17, 2022, from
 1020 https://www.sarmap.ch/tutorials/PS_Tutorial_V_0_9.pdf
- 1021 L3Harris. (2021, August). PS Tutorial – version 5.6. Retrieved April 17, 2022, from
 1022 https://www.sarmap.ch/tutorials/PS_v562.pdf
- 1023 Li, J., Wang, S., Miche, C., Russell, H., (2020). Surface deformation observed by InSAR shows
 1024 connections with water storage change in Southern Ontario. *Journal of Hydrology: Regional
 1025 Studies*. 27, 100661- 100672. doi:10.1016/j.ejrh.2019.100661
- 1026 Liang, C., Agram, P., Simons, M., Fielding, E., (2019). Ionospheric Correction of InSAR Time
 1027 Series Analysis of C-Band Sentinel-1 TOPS Data. *IEEE Transactions on Geoscience and
 1028 Remote Sensing*. 57 (9), 6755-6773. doi: 10.1109/TGRS.2019.2908494
- 1029 Love, R., Milne, G., Tarasov, L., Engelhart, S., Hijma, M., Latychev, K., Horton, B., and
 1030 Törnqvist, T., (2016). The contribution of glacial isostatic adjustment to projections of sea-
 1031 level change along the Atlantic and Gulf coast of North America. *Earth's Future*. 4 (10), 440-
 1032 464. doi:10.1002/2016EF000363
- 1033 Louisiana Department of Natural Resources – Strategic Online Natural Resources Information
 1034 System (SONRIS), (n.d.). Data of: Oil/Gas wells, Injection wells, and Water wells
 1035 registration [shp format], last visited June/2020. Retrieved from: <http://sonris->
 1036 www.dnr.state.la.us/gis/agsweb/IE/JSViewer/index.html?TemplateID=181
- 1037 Louisiana State University - Department of Geography and Anthropology (LSU), (n.d.). LiDAR
 1038 data distribution by “Atlas: The Louisiana Statewide GIS.” [LAS format], Baton Rouge, LA.
 1039 Last visited: June/2020. Retrieved from: <https://maps.ga.lsu.edu/lidar2000/>
- 1040 Mahapatra, P., der Marel, H., van Leijen, F., Samiei-Esfahany, S., Klees, R., Hanssen, R., (2018).
 1041 InSAR datum connection using GNSS-augmented radar transponders. *Journal of Geodesy*. 92
 1042 (1), 21-32. doi:10.1007/s00190-017-1041-y

- 1043 McCulloh, R., (2001) Active Faults in East Baton Rouge Parish; Louisiana. *Louisiana Geological*
1044 *Survey*. Public information series n. 8. Available at
1045 <https://www.lsu.edu/lgs/publications/products/public-information-series.php> (Accessed:
1046 January 2020).
- 1047 McCulloh, R., Heinrich, P., (2013). Surface faults of the south Louisiana growth-fault province.
1048 *The Geological Society of America*, Special Paper. 493, 37-49. doi: 10.1130/2012.2493(03).
- 1049 Milliman J., Haq B., (1996). “Sea-Level Rise and Coastal Subsidence: Towards Meaningful
1050 Strategies” In: Milliman, J.D., Haq, B.U. (eds) Sea-Level Rise and Coastal Subsidence.
1051 Coastal Systems and Continental Margins, vol 2. Springer, Dordrecht. 1-9. doi:10.1007/978-
1052 94-015-8719-8_1
- 1053 Morton, R., Busteri, N., Dennis K. (2002). Subsidence rates and associated wetland loss in south-
1054 central Louisiana. *Transactions of the Gulf Coast Association of Geological Societies*. 52,
1055 767-778.
- 1056 Nasreen, M. (2003) The effect of faults upon ground water flow in the BRF System. [master’s
1057 thesis]. [New Orleans (LA)] University of New Orleans. Available at
1058 <https://scholarworks.uno.edu/td/54> (Accessed: 1 June 2022)
- 1059 National Academies of Sciences, Engineering, and Medicine (NASEM), (2018). Understanding
1060 the Long-Term Evolution of the Coupled Natural-Human Coastal System: The Future of the
1061 U.S. Gulf Coast. Washington, DC: The National Academies Press. doi:10.17226/25108
- 1062 National Geodetic Survey (n.d.). Data from: Finding Survey Marks and Datasheets - LA[shp
1063 format], last visited January/2020. Retrieved from
1064 https://geodesy.noaa.gov/pub/DS_ARCHIVE/BETA_PRODUCTS/
- 1065 Nerem, R., Beckley, B., Fasullo, J., Hamlington, B., Masters, D., Mitchum, G., (2018). Climate-
1066 change–driven accelerated sea-level rise detected in the altimeter era. *Proceedings of the*
1067 *National Academy of Sciences*. 115 (9), 2022-2025. doi:10.1073/pnas.1717312115
- 1068 Nienhuis, J., Törnqvist, T, Jankowski1, K., Fernandes, A, Keogh, M., (2017). A new subsidence
1069 map for coastal Louisiana. *GSA Today*. 27 (9), 58-59. doi:10.1130/GSATG337GW.1
- 1070 Nissen, E., Krishnan, A., Arrowsmith, R., Saripalli, S., (2012). Three-dimensional surface
1071 displacements and rotations from differencing pre-and post-earthquake LiDAR point clouds.
1072 *Geophysical Research Letters*, 39 (16). doi:10.1029/2012GL052460
- 1073 PDAL Contributors, (2018). PDAL Point Data Abstraction Library. doi:10.5281/zenodo.2556738
- 1074 Pearson, C., Snay, R., (2013). Introducing HTDP 3.1 to transform coordinates across time and
1075 spatial reference frames. *GPS Solutions*. 17 (1), 1-15. doi: 10.1007/s10291-012-0255-y
- 1076 Pendleton, E., Barras, J., Williams, S., Twichell, D., (2010). Coastal vulnerability assessment of
1077 the Northern Gulf of Mexico to sea-level rise and coastal change. *U.S. Geological Survey*.
1078 Open-File Report. doi:10.3133/ofr20101146
- 1079 Penland, S. and Ramsey, K., (1990). Relative Sea Level Rise in Louisiana and the Gulf of
1080 Mexico: 1908-1988. *Journal of Coastal Research*. 6 (2), 323-342. Available at
1081 <https://www.jstor.org/stable/4297682> (Accessed: 20 Marzo 2021)
- 1082 Penland, S., Beall, A., and Waters, J., (2001) Environmental atlas of the Lake Pontchartrain
1083 Basin. *U.S. Geological Survey*. Open-File Report 02-206. Retrieve from
1084 <https://pubs.usgs.gov/of/2002/of02-206/intro/toc.html>

- 1085 Pindell, J. Kennan, L., (2009), Tectonic evolution of the Gulf of Mexico, Caribbean and northern
1086 South America in the mantle reference frame: An update. In *The Origin and Evolution of the*
1087 *Caribbean Plate, Geological Society, Special Publication.*, edited by Lorente, J., Pindell, J.
1088 328, 1–55. doi:10.1144/SP328.1.
- 1089 Puskas, C., Meertens, C., & Phillips, D. (2017). Hydrologic loading model displacements from
1090 the National and Global Data Assimilation Systems (NLDAS and GLDAS). *UNAVCO*
1091 *Geodetic Data Service Group*.
- 1092 Qiang, Y., Lam, N., (2016). The impact of Hurricane Katrina on urban growth in Louisiana: an
1093 analysis using data mining and simulation approaches. *International Journal of*
1094 *Geographical Information Science*. 30 (9), 1832-1852. doi:10.1080/13658816.2016.1144886
- 1095 QGIS Development Team, 2018. QGIS Geographic Information System. Open-Source Geospatial
1096 Foundation Project. [computer software] <http://qgis.osgeo.org>
- 1097 Robin, C., Craymer, M., Ferland, R., James, T., Lapelle, E., Piraszewski, M., Zhao, Y. (2020).
1098 NAD83v70VG: a new national crustal velocity model for Canada. Open File. doi:
1099 10.4095/327592
- 1100 Samieie-Esfahany, S., Hanssen, R., van Thienen-Visser, K., Muntendam-Bos, A., (2010). On the
1101 effect of Horizontal deformation on InSAR subsidence estimates. In *ESA Special*
1102 *Publication*. 677
- 1103 SARscape [computer software] (2021). Boulder, Colorado
- 1104 Sastry, N., (2009). Tracing the effects of hurricane Katrina on the population of New Orleans:
1105 The displaced New Orleans residents pilot study. *Sociological Methods and Research*. 38 (1),
1106 171-196. doi:10.1177/0049124109339370
- 1107 Sawyer, D., Buffler, R., Pilger Jr., R., (1991), “The crust under the Gulf of Mexico basin” In *The*
1108 *Gulf of Mexico Basin, Geological Society of America*, ed. by A. Salvador. 53–72.
1109 doi:10.1130/DNAG-GNA-J.53
- 1110 Scott, C., Arrowsmith, J., Nissen, E., Lajoie, L., Maruyama, T., Chiba, T., (2018). The M7 2016
1111 Kumamoto, Japan, Earthquake: 3-D deformation along the fault and within the damage zone
1112 constrained from Differential Lidar Topography. *Journal of Geophysical Research: Solid*
1113 *Earth*, 123 (7) 6138-6155. doi:10.1029/2018JB015581
- 1114 Scott, C., Phan, M., Nandigam, V., Crosby, C., & Arrowsmith, R. (2020). On-Demand 3D
1115 topographic differencing implemented in OpenTopography (Version 1.1.0) [Computer
1116 software]. https://github.com/OpenTopography/3D_Differencing
- 1117 Shen, Z., Dawers, N., Törnqvist, T., Gasparini, N., Hijma, M., and Mauz, B. (2017). Mechanism
1118 of late Quaternary fault throw-rate variability along the north central Gulf of Mexico coast:
1119 implication for coastal subsidence. *Basin Research*. 29 (5), 557-570. doi:10.1111/bre.12184
- 1120 Shepard, D., (1968). A two-dimensional interpolation function for irregularly spaced data.
1121 *Proceedings of the 1968 ACM National Conference*. 517 – 524.
1122 <https://doi.org/10.1145/800186.810616>
- 1123 Shirzaei, M., Ellsworth, W., Tiampo, K., Gonzalez, P., Manga, M., (2016). Surface uplift and
1124 time-dependent seismic hazard due to fluid injection in eastern Texas. *Science*. 353 (6306),
1125 1416-1419. doi:10.1126/science.aag0262

- 1126 Shirzaei, M., Freymuller, J., Tornqvist, T., Galloway, D., Dura, T., Minderhoud, P., (2021).
1127 Measuring, modeling and projecting coastal land subsidence. *Nature Reviews Earth and*
1128 *Environment*. 2(1), 40-58. doi: 10.1038/s43017-020-00115-x
- 1129 Snay, R., Freymuller, J., Pearson, C., (2013). Crustal Motion Models Developed for Version 3.2
1130 of the Horizontal Time-Dependent Positioning Utility. *Journal of Applied Geodesy*. 7 (3),
1131 173-190. doi: 10.1515/jag-2013-0005
- 1132 Stevenson, D. A., & Agnew, J. D. (1988). Lake Charles, Louisiana, earthquake of 16 October
1133 1983. *Bulletin of the Seismological Society of America*. 78 (4), 1463-1474.
1134 doi:10.1785/BSSA0780041463
- 1135 Teatini, P., Gambolati, G., Ferronato, M., Serrati, A., Walters, D., (2011). Land uplift due to
1136 subsurface fluid injection. *Journal of Geodynamics*. 51 (1), 1-16.
1137 doi:10.1016/j.jog.2010.06.001
- 1138 Tomaszewski, D., Lovelace, J., Ensminger, P., (2002). Water withdrawals and trends in
1139 groundwater levels and stream discharge in Louisiana. *Louisiana Department of*
1140 *Transportation and Development, and U.S. Geological Survey*, technical report No. 68.
- 1141 Turner, R., Rabalais, N., (2018). “The Gulf of Mexico.” In *World Seas: An Environmental*
1142 *Evaluation (Second Edition)*, Academic Press -Elsevier, edited by Sheppard, C, 445-464.
1143 doi:10.1016/B978-0-12-805068-2.09994-0
- 1144 United States Army Corps of Engineers (USACE) (2001). Data from: Raw LIDAR Elevation
1145 Data, UTM 15 NAD83, Louisiana FEMA Project - Phase 1: Amite River Basin. last visited
1146 June/2020 Retrieve from: <https://maps.ga.lsu.edu/lidar2000/>
- 1147 United States Geological Survey (USGS) (2019), USGS Lidar Point Cloud LA Amite 2018, [LAZ
1148 format], last visited July/2022. Retrieve from:
1149 [https://rockyweb.usgs.gov/vdelivery/Datasets/Staged/Elevation/LPC/Projects/USGS_LPC_L](https://rockyweb.usgs.gov/vdelivery/Datasets/Staged/Elevation/LPC/Projects/USGS_LPC_LA_Amite_2018_LAS_2019/)
1150 [A_Amite_2018_LAS_2019/](https://rockyweb.usgs.gov/vdelivery/Datasets/Staged/Elevation/LPC/Projects/USGS_LPC_LA_Amite_2018_LAS_2019/)
- 1151 U.S. Census Bureau. (2003, October). Louisiana 2000 – Population and Housing units counts
1152 (Report No. PHC-3-20). Retrieved from
1153 <https://www2.census.gov/library/publications/2003/dec/phc-3-20.pdf>
- 1154 U.S. Census Bureau. (2012, July). Louisiana 2010 – Population and Housing units counts (Report
1155 No. CPH-2-20). Retrieved from
1156 <https://www2.census.gov/library/publications/decennial/2010/cph-2/cph-2-20.pdf>
- 1157 U.S. Census Bureau. (2021, August). 2020 Population and Housing State Data. Retrieved from
1158 [https://www.census.gov/library/visualizations/interactive/2020-population-and-housing-state-](https://www.census.gov/library/visualizations/interactive/2020-population-and-housing-state-data.html)
1159 [data.html](https://www.census.gov/library/visualizations/interactive/2020-population-and-housing-state-data.html)
- 1160 Vahdat-Aboueshagh, H., Tsai, F., (2021). Constructing large-scale complex aquifer systems with
1161 big well log data: Louisiana model. *Computers and Geosciences*. 148, 104687.
1162 doi:10.1016/j.cageo.2021.104687
- 1163 Walter, J. I., Dotray, P. J., Frohlich, C., & Gale, J. F. (2016). Earthquakes in northwest Louisiana
1164 and the Texas–Louisiana border possibly induced by energy resource activities within the
1165 Haynesville shale play. *Seismological Research Letters*. 87(2A), 285-294.
1166 doi:10.1785/0220150193
- 1167 Wheaton, J., Brasington, J., Darby, S., Sear, D., (2010). Accounting for uncertainty in DEMs
1168 from repeat topographic surveys: improved sediment budgets. *Earth Surface processes and*

- 1169 *Landforms*. 35 (2), 136-156. doi:10.1002/esp.1886 [computer software]
1170 <https://github.com/Riverscapes/gcd>
- 1171 Wheaton, J., (2018). Principles of topographic change detection. EarthCube Advancing the
1172 Analysis of HRT Workshop Advancing the Analysis of High-Resolution Topography,
1173 Broomfield, CO. August 21-24.
1174 https://www.youtube.com/watch?v=QIoK52W5sUM&ab_channel=OpenTopography (last
1175 accessed November 10, 2020)
- 1176 White, E. (2017). Water Resources of the Southern Hills Regional Aquifer System, Southeastern
1177 Louisiana. *U.S. Geological Survey Fact Sheet* 2017–3010. doi:10.3133/fs20173010
- 1178 Yu, C., Penna, N., Li, Z., (2017). Generation of real-time mode high-resolution water vapor fields
1179 from GPS observations. *Journal of Geophysical Research: Atmospheres*. 122, 2008-2025.
1180 doi: 10.1002/2016JD025753
- 1181 Zhong, W., Chu, T., Tissot, P., Wu, Z., Chen, J., Zhang, H., (2022). Integrated coastal subsidence
1182 analysis using InSAR, LiDAR and land cover data. *Remote Sensing of Environment*. 282.
1183 doi: 10.1016/j.rse.2022.113297